J. Fluid Mech. (2022), *vol.* 937, A26, doi:10.1017/jfm.2022.113

Open-channel flow over evolving subaqueous ripples

Aman G. Kidanemariam[1],†, **Markus Scherer**[2] **and Markus Uhlmann**[2]

[1]Department of Mechanical Engineering, The University of Melbourne, Victoria 3010, Australia

[2]Institute for Hydromechanics, Karlsruhe Institute of Technology, 76131 Karlsruhe, Germany

(Received 25 May 2021; revised 5 November 2021; accepted 31 January 2022)

We have numerically investigated the turbulent flow and sediment grain motion in an open-channel flow configuration over a subaqueous sediment bed featuring two-dimensional transverse ripples at moderate Reynolds number and super-critical Shields number values. The simulation data, which were generated by means of particle-resolved direct numerical simulation, are the same as in our previous work (Kidanemariam & Uhlmann, *J. Fluid Mech.*, vol. 818, 2017, pp. 716–743). By carefully choosing the computational box sizes, we were able to accommodate single ripple units which form over an initially flat sediment bed at a wavelength equal to the domain length. The ripples then evolve into their asymmetric shape relatively quickly and eventually migrate downstream steadily while maintaining their shape and size. In the present study, using a ripple-conditioned phase-averaging procedure, we are able to obtain novel insights into the evolution of the turbulent flow and particle motion over the bedforms, in particular the spatial structure of the basal shear stress and its relation to the particle flow rate. Our analysis confirms that the boundary shear-stress maximum is located upstream of the ripple crest, while the particle flow rate is essentially in phase with the ripple topology, with an average phase difference between the two in the range of 18–19 particle diameters for the considered parameter values. We were further able to confirm the link between the sediment flux relaxation behaviour and the observed shear-stress/geometry lag, by direct evaluation of the saturation length scale.

Key words: sediment transport, particle/fluid flow, turbulence simulation

1. Introduction

One fascinating phenomenon of sediment transport is the formation of patterns, such as ripples, dunes or ridges. These sediment patterns have important implications for many environmental and industrial applications, for example, they influence the rate of sediment

---

† Email address for correspondence: aman.kidanemariam@unimelb.edu.au

© The Author(s), 2022. Published by Cambridge University Press. This is an Open Access article, distributed under the terms of the Creative Commons Attribution licence (https://creativecommons.org/licenses/by/4.0/), which permits unrestricted re-use, distribution, and reproduction in any medium, provided the original work is properly cited.

transport in a given river. Although the problem of sediment pattern formation has been subject to extensive studies over the past several decades, a number of fundamental questions still remain unanswered due to the inherently complex dynamics (Best 2005; Andreotti & Claudin 2013; Charru, Andreotti & Claudin 2013). A key challenge is the accurate description of the driving turbulent flow over the bedforms and its interplay with the sediment bed. In particular, faithful description of the spatial structure of the boundary shear stress and its relation to the sediment flux remains an open problem. The latter defines the morphological evolution process of sedimentary patterns and is an important ingredient in many sediment transport models (Seminara 2010; Charru *et al.* 2013).

The present work is concerned with statistically two-dimensional transverse subaqueous bedforms worked by a uni-directional turbulent flow. The flow evolving over such train of bedforms is statistically non-homogeneous and entails complex interaction with the sediment bed (see e.g. review by Best 2005). To simplify the problem, most of previous experimental and numerical studies of the configuration have considered flow over fixed dunes with imposed geometry (see e.g. McLean & Smith 1986; Nelson, McLean & Wolfe 1993; McLean, Nelson & Wolfe 1994; Bennett & Best 1995; Stoesser *et al.* 2008; Omidyeganeh & Piomelli 2011). Although such studies have been useful in elucidating the key features of the flow, they fail to provide information on the mutual interaction between the flow and the evolving sediment bed composed of mobile grains. Similarly, theoretical studies that investigate the hydro-morphodynamic instability and evolution of the sediment bed invoke a disparity in time scales between the flow and the bed shape evolution and assume a fixed wavy bottom perturbation to solve the fluid flow (see e.g. Kennedy 1963; Richards 1980; Colombini & Stocchino 2011). Customarily, the flow solution is based on the seminal work by Jackson & Hunt (1975), which is an extension of the asymptotic solutions of the laminar flow over a bump by Benjamin (1959) to the turbulent regime (see reviews by Belcher & Hunt (1998) and Charru *et al.* (2013) for a detailed account). An important outcome of these studies is that the flow can be considered as a layered structure: an outer inviscid region far from the bottom and an inner ‘logarithmic’ region where turbulent stresses and viscosity are important. In the theoretical analysis, the matching of the two layers reveals a phase advance of the boundary shear stress with respect to the topography. In the context of sediment transport, the phase difference between the shear stress and the bottom is the main destabilising mechanism of a perturbed erodible bed. A balance between this destabilising mechanism and other stabilising effects such as gravity (Engelund & Fredsoe 1982) and sediment-bed relaxation effects (Charru 2006; Fourrière, Claudin & Andreotti 2010) is believed to result in the initiation of bed patterns at a certain preferred wavelength. However, finite-amplitude effects beyond the linear regime, such as flow separation downstream of the ripple crest, cannot be accounted for by the above methods and a theoretical description is still an open issue (Charru & Luchini 2019).

Concerning the sediment bed, the majority of the algebraic models that relate the fluid shear stress with the sediment flux are developed for the equilibrium state. The transient behaviour of the sediment bed is usually treated by assuming that the bed responds to changes in flow conditions instantaneously. This assumption allows one to relate the local shear stress to the local particle flow rate. However, it is well recognised that the sediment bed needs some temporal/spatial lag to adapt to a change in the flow conditions due to its inertia (Sauermann, Kroy & Herrmann 2001; Charru 2006). The sediment-bed relaxation behaviour, usually expressed in terms of a characteristic saturation length scale, has been argued to be a stabilising factor during sediment-bed instability and it thereby controls the scaling of initial aeolian/subaqueous bedforms. Although models that include such a sediment relaxation effect through the introduction of a separate differential equation for the particle number density or for the particle flux (Valance

2005; Charru 2006; Fourrière *et al.* 2010) into the stability analysis have been partially successful, they still fall short of accurately determining the initial ripple wavelength (Langlois & Valance 2007; Ouriemi, Aussillous & Guazzelli 2009). The limitation is attributed to the lack of a fully appropriate model for the saturation length that stems from the simplified description of the complex particle dynamics near and inside the bed. Moreover, the two-way feedback mechanism between the sediment grains and the shearing flow is usually ignored. The saturation length encompasses a wide spectrum of length scales as a consequence of simultaneously occurring particle transport modes (rolling, sliding, saltation, etc.) and dynamical mechanisms (rebounding, inter-particle collision, particle–turbulence interaction, etc.). A dominant transport mode or mechanism is usually selected for a given regime. For instance, in the particle inertia dominated regime, the relaxation is believed to scale with the drag length l_d, which is often based on Stokes drag, i.e. $l_d \approx (\rho_p/\rho_f)D$, where ρ_p/ρ_f and D are the fluid-to-particle density ratio and particle diameter, respectively (Fourrière *et al.* 2010). Other saturation length models account for different hydrodynamic and granular bed interactions and introduce other length scales, such as the deposition length that represents the distance travelled by particles (moving at a certain characteristic velocity), during their deposition time $t_d \sim D/u_s$, where u_s is the particle settling velocity (Charru & Hinch 2006; Charru 2006). In the context of aeolian sand transport (very large particle-to-fluid density ratios), the saltation length, which represents the distance covered by saltating grains during their flight time, is considered to be the governing length scale (Sauermann *et al.* 2001). In an attempt to address the above shortcomings, Pähtz *et al.* (2013, 2014, 2015) propose a more elaborate and fairly complex model with several adjustable parameters that accounts for additional mechanisms such as the relaxation associated with the fluid–particle and inter-particle interactions.

Carrying out highly resolved experimental measurements of both the flow and the erodible sediment-bed motion (in the presence of bedforms) is a difficult task and available data are scarce (see e.g. Charru & Franklin 2012; Rodrıguez-Abudo & Foster 2014; Leary & Schmeeckle 2017; Frank-Gilchrist, Penko & Calantoni 2018). Notably, Charru & Franklin (2012) report measurements of the flow over isolated evolving barchan dunes in a confined channel flow experiment. They assessed the layered structure of the flow over the barchan as predicted by the asymptotic theories, ignoring the re-circulating flow downstream of the barchan brink (measurements of the three-dimensional flow were taken at the symmetry plane of the barchan). However, the experiments did not allow access to the relationship between the local shear stress and the particle flux. Concerning the sediment-bed relaxation behaviour, there is currently no direct experimental measurement of the saturation length for subaqueous sediment transport available (Andreotti & Claudin 2013; Duran Vinent *et al.* 2019). The majority of field and laboratory measurements as well as theoretical modelling of the saturation length have been for the aeolian sediment transport regime (Andreotti, Claudin & Douady 2002; Lajeunesse, Malverti & Charru 2010; Claudin, Wiggs & Andreotti 2013; Pähtz *et al.* 2015; Selmani *et al.* 2018; Gadal *et al.* 2020; Lü *et al.* 2021). In these studies, saturation length measurements are reported by retrieving the grain flux indirectly from the measurement of bed elevation profiles through the sediment mass conservation equation.

Faithful numerical simulation of sediment transport phenomena is very challenging. It has thus been common practice to simplify the description of the flow and/or the sediment-bed dynamics. On the one hand, there are studies that fully resolve the turbulent flow while describing the sediment bed via continuum modelling (see e.g. Chou & Fringer 2010; Khosronejad & Sotiropoulos 2014; Zgheib *et al.* 2018; Zgheib & Balachandar 2019) or via point-particle based Lagrangian modelling (Finn, Li & Apte 2016; Guan *et al.* 2021).

Other studies, on the other hand, sufficiently account for the dynamics of the sediment bed (based on discrete-element models) but without resolving the turbulent background flow (Durán, Andreotti & Claudin 2012; Schmeeckle 2014; Maurin *et al.* 2015). Both modelling approaches rely on some sort of (semi-)empirical expression to couple the fluid problem with the morphodynamic one. Recent progress in particle-resolving direct numerical simulations (DNS) that account for both the flow and individual grain motion without modelling the fluid–particle interaction have started to shed light on the grain-scale dynamics and the interaction of an evolving thick sediment bed with the driving turbulent flow (see e.g. Kidanemariam & Uhlmann 2014*a*; Vowinckel, Kempe & Fröhlich 2014; Kidanemariam 2015; Kidanemariam & Uhlmann 2017; Mazzuoli, Kidanemariam & Uhlmann 2019; Mazzuoli *et al.* 2020; Scherer, Kidanemariam & Uhlmann 2020; Jain, Tschisgale & Fröhlich 2021).

The objective of the present work is to investigate, with the aid of particle-resolved DNS data, the spatial structure of the turbulent flow and the particle motion over a train of two-dimensional transverse bedforms, and to address its correlation with the evolving sediment bed. In our recent work (Kidanemariam & Uhlmann 2017, hereafter termed as KU2017), we have carried out extensive simulations of subaqueous pattern formation in a turbulent open-channel flow configuration. The study in KU2017 was devoted to the initiation and evolution aspects of the sediment patterns. In the present contribution, we revisit the simulation data in KU2017 and analyse the fluid flow and particle motion. In particular, we analyse the spatial structure of the bed shear stress and its relation to the particle flow rate. To this end, we have performed ripple-conditioned phase averaging of the fluid flow that takes into account the spatio-temporal variability of the sediment bed. Let us note that the conditions of the simulations reported in KU2017 (varying the computational box size for a single physical parameter point) allowed systematic investigation of the different ripple evolution stages. That is, the temporal growth of the ripple size was systematically ‘frozen’ by limiting the computational domain length that accommodates only a single ripple unit. The formed ripples were thereby constrained to migrate steadily, maintaining their asymmetric shape at a mean wavelength equal to the length of the domain. The strategy allows us to accumulate sufficient statistics for detailed analysis of the interaction between the turbulent flow and the evolving ripple unit. The paper is organised as follows: in § 2 we provide a short description of the computational set-up and numerical solution strategy. The evolution of the bulk flow characteristics in response to the evolution of the bed is presented in § 3. In § 4 we present phase-averaged statistics including that of the boundary shear stress and evaluate the phase lag between the bed shear stress and the sediment flux. The main findings of the paper are summarised and discussed in § 5.

2. Flow configuration, simulation strategy and numerical method

We consider an open-channel flow of an incompressible viscous fluid with a density ρ_f and viscosity ν over an evolving sediment bed, as shown schematically in figure 1. The sediment bed is composed of spherical particles of diameter D and density ρ_p. A Cartesian coordinate system (x, y, z) is defined, x and z representing the streamwise and spanwise (lateral) directions respectively while y is the vertical direction. The corresponding Eulerian fluid and Lagrangian sediment particle velocity vectors are defined as $\boldsymbol{u}_f = (u_f, v_f, w_f)$ and $\boldsymbol{u}_p = (u_p, v_p, w_p)$, respectively. Mean flow is directed in the positive x direction and the vector of gravitational acceleration $\boldsymbol{g}$ points in the negative y direction.

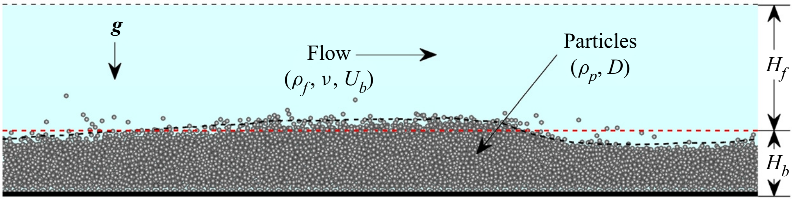

Figure 1. Schematics of an open-channel flow of a fluid with density ρ_f and viscosity ν over an evolving sediment bed. The sediment bed is represented by a large number of freely moving spherical particles of diameter D and density ρ_p.

The mean fluid height is denoted as H_f while the corresponding mean sediment-bed thickness is denoted as H_b.

The simulation data analysed in the present study are identical to those reported in KU2017. Specifically, data corresponding to the ripple featuring cases termed H4[3], H6 and H7 therein, are considered for the phase-averaging analysis. Details of the simulation campaign and numerical method used can be found in KU2017. A short description is provided here for completeness. The simulations were carried out in bi-periodic three-dimensional computational boxes (periodic in the streamwise and spanwise directions). No-slip and free-slip conditions were imposed at the bottom and top planes of the channel, respectively. The flow was driven by a streamwise pressure gradient imposing a desired constant mean flow rate q_f. The fluid flow is described by the bulk Reynolds number $Re_b = u_b H_f/\nu$ or equivalently the friction Reynolds number $Re_\tau = u_\tau H_f/\nu$, where $u_b \equiv q_f/H_f$ and u_τ are the bulk and friction velocities respectively. Note that u_τ is evaluated *a posteriori* from the mean total shear stress evaluated at a wall-normal location of the mean fluid–bed interface $y = H_b$. The location of the interface between the fluid and the sediment bed has been determined based on the threshold value of the solid volume fraction. Details of the extraction of the fluid–bed interface and precise definitions of H_f, H_b and u_τ can be found in KU2017. Important parameters describing the submerged sediment bed include: the particle-to-fluid density ratio ρ_p/ρ_f, the length scale ratios H_f/D and $D^+ \equiv D u_\tau/\nu$ and a ratio between the gravity and viscous forces described by the Galileo number $Ga = U_g D/\nu$, where U_g is the gravitational velocity scale $U_g = \sqrt{(\rho_p/\rho_f - 1)|\boldsymbol{g}|D}$. Finally, let us define the Shields number, which is the ratio between the fluid shear force at the bed and the submerged weight of a particle, as $\theta \equiv (u_\tau/U_g)^2$ (Shields 1936). The values of these physical parameters are listed in table 1. Note that the three simulation cases have identical values of the imposed physical parameters. As shown in table 2, the only difference, in terms of imposed quantities, is the streamwise extent of the simulation box. Case H4 has a domain length of approximately four times the mean fluid height, while that of H6 and H7 is approximately six and seven times the mean fluid height, respectively. These differences in domain length result in different sizes of the accommodated ripple units that in turn result in somewhat different values of the derived parameters such as Re_τ, θ and D^+ (the evolution process is discussed in more detail in § 3).

The numerical method used to carry out the simulations is based upon the immersed boundary technique of Uhlmann (2005) for the treatment of the fluid–solid interactions, wherein the incompressible Navier–Stokes equations are solved with a second-order finite-difference method throughout the entire computational domain, adding a localised force term that serves to impose the no-slip condition at the fluid–solid interface. Individual sediment particle motion is obtained via integration of the Newton–Euler

Case	Re_b	Re_τ	ρ_p/ρ_f	Ga	H_f/D	D^+	θ
H4	3011	264	2.5	28.37	25.14	10.46	0.14
H6	3011	303	2.5	28.37	25.47	11.90	0.18
H7	3011	309	2.5	28.37	25.30	12.22	0.19

Table 1. Physical parameters of the simulations; Re_b and Re_τ are the bulk and friction Reynolds numbers, respectively; ρ_p/ρ_f is the particle-to-fluid density ratio; Ga and θ are the Galileo number and the Shields number, respectively.

Case	$(L_x \times L_y \times L_z)/D$	$(L_x \times L_y \times L_z)/H_f$	Δx^+	$D/\Delta x$	N_p	N_p^{fix}	T_{obs}/T_b	T_{obs}^s/T_b
H4	$102.4 \times 38.4 \times 76.8$	$4 \times 1.5 \times 3$	1.05	10	86 645	7314	851	557
H6	$153.6 \times 38.4 \times 76.8$	$6 \times 1.5 \times 3$	1.19	10	127 070	11 040	918	583
H7	$179.2 \times 38.4 \times 76.8$	$7 \times 1.5 \times 3$	1.22	10	150 521	12 972	976	574

Table 2. Numerical parameters of the simulations; L_i is the domain length in the ith direction. The grid spacing is uniform in all directions, i.e. $\Delta x = \Delta y = \Delta z$; N_p is the number of particles in the simulations, out of which N_p^{fix} are fixed in space at the channel bottom to create a rough boundary; T_{obs} is the total observation time of each simulation starting from the release of the moving particles. Ripple-conditioned statistics are computed over the steady dune propagation interval T_{obs}^s; $T_b = H_f/u_b$ is the bulk time unit.

equations for rigid body motion, driven by the hydrodynamic force (and torque) as well as gravity and the force (torque) resulting from solid–solid contact. The inter-particle collision process is described via a discrete element model (DEM) based on the soft-sphere approach (Kidanemariam & Uhlmann 2014*b*). A pair of particles is defined as 'being in contact' when the smallest distance between their surfaces, $\varDelta$, becomes smaller than a force range $\varDelta_c$. The resulting contact force is then the sum of an elastic normal component, a normal damping component and a tangential frictional component. The elastic part of the normal force component is a linear function of the penetration length $\delta_c \equiv \varDelta_c - \varDelta$, with a stiffness constant k_n. The normal damping force is a linear function of the normal component of the relative velocity between the particles at the contact point with a constant coefficient c_n. The tangential frictional force (the magnitude of which is limited by the Coulomb friction limit with a friction coefficient μ_c) is a linear function of the tangential relative velocity at the contact point, again formulated with a constant coefficient denoted as c_t. Since the characteristic collision time is typically orders of magnitude smaller than the time step of the flow solver, the numerical integration of the equations for the particle motion is carried out adopting a sub-stepping technique, freezing the hydrodynamic forces acting upon the particles between successive flow field updates. A detailed description of the collision model and the corresponding parameter values as well as extensive validation and convergence studies can be found in Kidanemariam & Uhlmann (2014*b*).

3. Evolution of the flow and sediment bed

The simulations were initiated by first developing a turbulent flow over a macroscopically flat bed composed of pseudo-randomly packed stationary particles. The coupled fluid–solid simulations were then switched on by allowing the particles to move (except the N_p^{fix} particles that are fixed in space at the channel bottom to create a

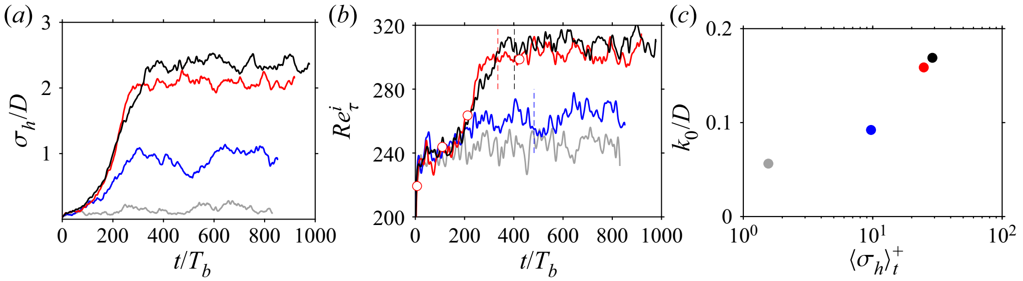

Figure 2. (*a*) Time evolution of the root-mean-square sediment-bed-height fluctuation normalised by the particle diameter (data reproduced from KU2017). (*b*) The corresponding evolution of the instantaneous friction Reynolds number for each of the cases. The vertical dashed lines indicate the start time of the steady ripple propagation interval over which statistics are accumulated. The circle symbols along the Re_τ evolution of case *H*6 correspond to the time instances of the visualisations in figure 3. (*c*) The hydrodynamic roughness length k_0 as a function of the mean sediment-bed-height fluctuation $\langle\sigma_h\rangle_t^+$. In all plots, lines and symbols are colour coded as follows: grey, featureless bedload; blue, H4; red, H6; black, H7.

rough boundary). Subsequently, the macroscopically flat sediment bed gets perturbed as a result of the ensuing particle erosion and deposition processes caused by the shearing turbulent flow above. For the conditions of our simulations, the sediment-bed perturbations ultimately evolve towards statistically two-dimensional transverse bedforms that propagate downstream at a constant migration velocity and with a wavelength equal to the domain length. The bed evolution in turn modifies the flow from its initial statistically one-dimensional state towards a two-dimensional flow with strong spatio-temporal correlation with the morphology of the underlying bed. Let us first look at the evolution of bulk sediment and fluid flow properties. In figure 2(*a*), we reproduce from KU2017 the temporal evolution of the root-mean-square (r.m.s.) sediment-bed height σ_h for the three cases considered in the present study (for reference, the evolution of the featureless bedload transport case H3 is also plotted). After an initial exponential growth, σ_h attains a statistically constant value. The corresponding temporal evolution of the instantaneous friction Reynolds number ${Re_\tau}^i$ is also provided in figure 2(*b*). Here, ${Re_\tau}^i$ is computed from the instantaneous value of the imposed driving pressure gradient $\varPi$ that is required to maintain the desired constant flow rate. The latter is obtained from the integration of the streamwise momentum equation across the whole computation domain that, subject to the incompressibility constraint, reduces to

$$\varPi(t) = -\frac{1}{L_x L_y L_z}\sum_{l=1}^{N_p} I_{fix}^{(l)}\left(F_{p,x}^{H(l)}(t) + F_{p,x}^{C(l)}(t)\right) - \frac{1}{L_y}\langle\tau^W\rangle_{xz}(t), \tag{3.1}$$

where $F_{p,x}^{H(l)}$ and $F_{p,x}^{C(l)}$ are the streamwise components of the hydrodynamic and collision forces acting on the *l*th particle, respectively. Here, $I_{fix}^{(l)}$ is an indicator function that has a value of unity if the *l*th particle is held fixed and zero otherwise; $\langle\tau^W\rangle_{xz}$ is the instantaneous average shear stress at the bottom smooth wall beneath the stationary particles and has a negligible contribution due to the practically zero velocity gradients therein. Thus, the driving volume force is is entirely balanced by the total resistance force exerted by the stationary particles located beneath the mobile sediment layer. The friction Reynolds number correspondingly increases from an initial value of ${Re_\tau}^i \approx 190$ to the average values Re_τ (measured in the asymptotic regime), as reported in table 1. Note that the

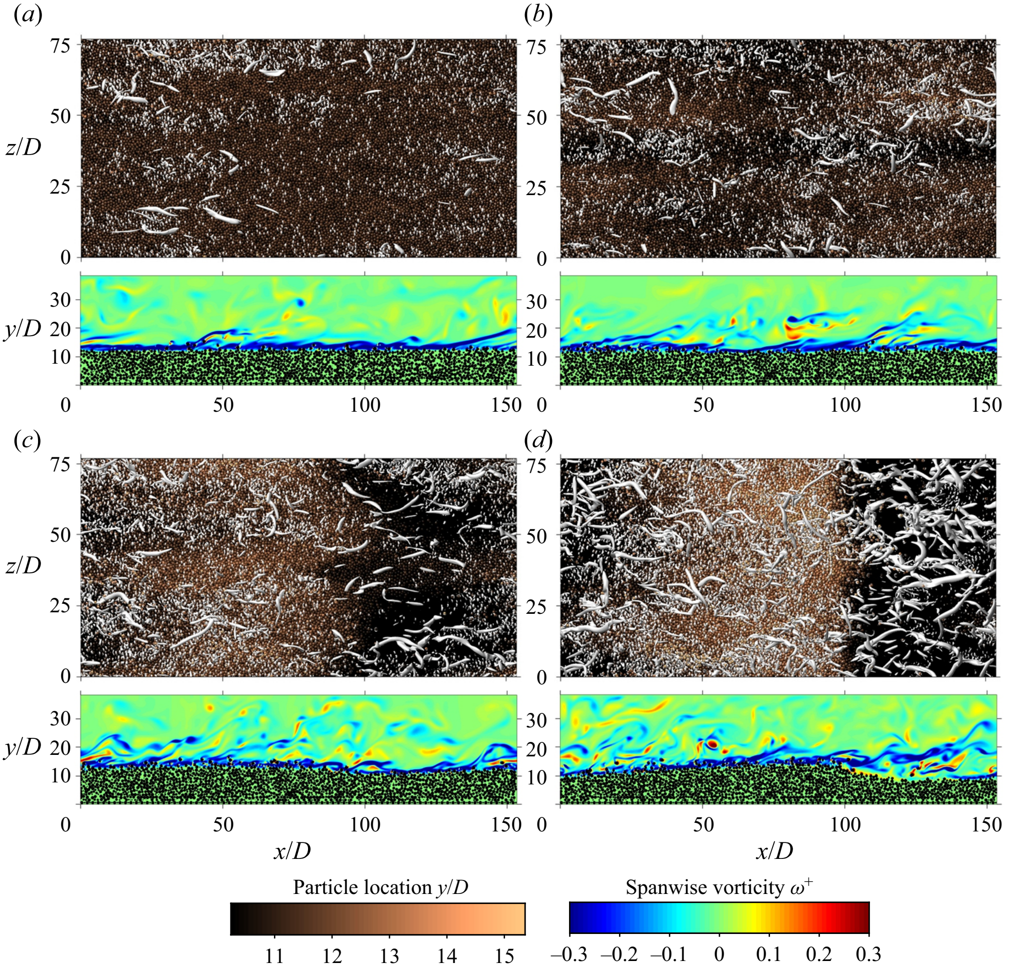

Figure 3. Instantaneous snapshots of the flow field and particle positions of case H6 at times (*a*) $t/T_b \approx 7$, (*b*) $t/T_b \approx 110$, (*c*) $t/T_b \approx 212$ and (*d*) $t/T_b \approx 423$. The top-view panels show turbulent vortical structures (grey surfaces) over the sediment-bed particles that are coloured based on their wall-normal location. The side-view panels show the corresponding spanwise vorticity on an x–y plane located at $z = 0$ (the intersection region of particles and the plane is shown in black).

initial Re_τ value corresponds to the turbulent flow over the macroscopically flat bed prior to the start of the coupled fluid–solid simulations. Since the total number of the heavier-than-fluid spherical particles remains the same during the simulation period, the average sediment-bed height remains essentially constant with time (except for some initial short dilation interval). Thus the temporal increase of ${Re_\tau}^i$ is entirely a consequence of the increasing roughness height of the bedforms. This is further confirmed by the direct correspondence of the evolution of the r.m.s. sediment-bed height and ${Re_\tau}^i$.

One way of quantifying the feedback of the evolving sediment bed on the turbulent flow is to express the mean fluid velocity profile U_f in the logarithmic layer through the definition of a hydrodynamic roughness height k_0 as $U_f^+ = 1/\kappa \log((y - y_0)/k_0)$, where $\kappa = 0.41$ is the von Kármán coefficient and y_0 is some reference origin (Jiménez 2004). The majority of the available sediment morphodynamic models strongly depend on the roughness parameter k_0 (Charru *et al.* 2013) and make use of classical correlations of k_0 versus particle Reynolds number D^+ that are obtained, for example, from flows over stationary roughness elements (see e.g. Fourrière *et al.* 2010; Colombini & Stocchino 2011; Duran Vinent *et al.* 2019). However, as is demonstrated in figure 2(*c*), the motion of the sediment bed and the evolving ripples substantially increase the value of k_0 for essentially the same value of D^+.

Figure 3 shows sample instantaneous flow visualisations of case H6 at selected times, spanning the duration from the first instants of the bed instability (several bulk time units after particles are released), through the initial evolution stage and up to the steady ripple propagation interval. The snapshots clearly highlight the coupled spatio-temporal evolution of the sediment bed and turbulent flow above. It can be seen that the intensity and density of the coherent structures evolve to be the highest in regions downstream of the crest of the forming transverse bedforms. It is the contrary for regions of the flow above and upstream of the crest where turbulence activity is weaker. The non-homogeneous spatial distribution of the vortices visually corroborates previous experimental and numerical investigation of the flow over fixed dunes (McLean *et al.* 1994; Stoesser *et al.* 2008; Omidyeganeh & Piomelli 2011). It is known that the flow over developed two-dimensional bedforms possesses distinct regions that can be summarised into an accelerating and a decelerating flow region upstream and downstream of the dune crest respectively, a shear layer region downstream of the dune crest where flow separation occurs, a re-circulation region extending several dune heights downstream of the crest and bounded by the shear layer and a developing boundary layer region attached to the stoss side of the dune (Best 2005). The snapshots illustrate the complexity of the flow in this configuration. Moreover, the visualisations additionally show that large coherent structures leave their footprint in the morphology of the bed, visible as slight longitudinal ridges and troughs superposed on the transverse bedforms. The mechanism behind the formation of these ridges is equally fascinating (cf. Scherer *et al.* 2021) but is outside the scope of the present work.

4. Ripple-conditioned fluid flow and particle motion

Here, we present an analysis of the turbulent flow field and particle motion that develops over the time-dependent sediment bed. We have performed ripple-conditioned phase averaging of the flow field in the steady ripple propagation interval. The reader is referred to Appendix A for the precise definition of the space- and time-averaging operators, while Appendix B details the phase averaging procedure and definition of notations used in subsequent sections.

4.1. *Spatial structure of the mean flow*

The streamwise and wall-normal components of the phase-averaged fluid velocity vector $\tilde{\boldsymbol{U}}_f \equiv (\tilde{U}_f, \tilde{V}_f)$ and the corresponding particle velocity vector $\tilde{\boldsymbol{U}}_p \equiv (\tilde{U}_p, \tilde{V}_p)$ for case H7 are shown in figure 4 (cf. Appendix B for the definitions of $\tilde{\boldsymbol{U}}_f$ and $\tilde{\boldsymbol{U}}_p$). The figures highlight significant modulation of the flow by the ripple morphology. As is expected, below the fluid–bed interface, mean fluid and particle velocities are found to be negligibly small. Above the fluid–bed interface, on the other hand, velocities of both phases show large spatial variations that are seen to be strongly correlated with the ripple geometry. At and near the interface, $\tilde{U}_f$ is observed to be higher in the region above the crest of the ripple. The value of $\tilde{U}_f$ decreases downstream of the crest, attaining negative values in the re-circulation region highlighted by the negative $\tilde{U}_f$ contour shown

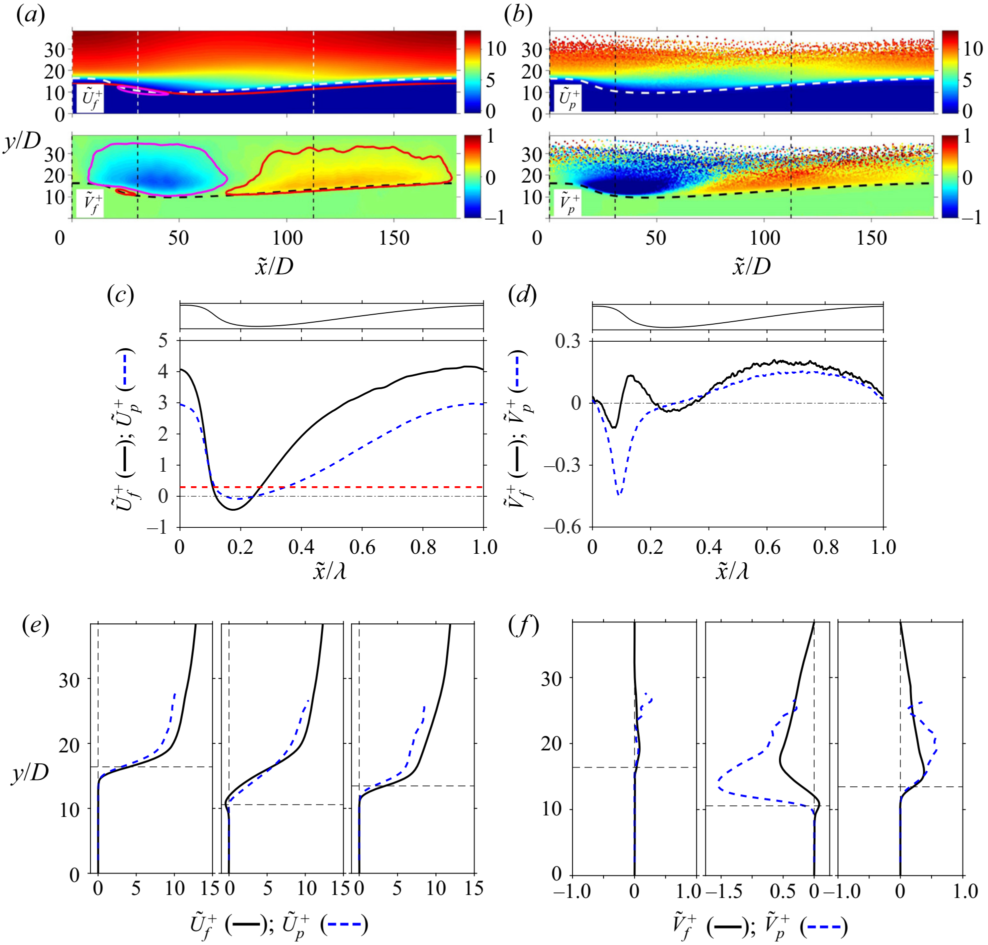

Figure 4. (*a*) Phase-averaged fluid velocity components ($\tilde{U}_f{}^+$, $\tilde{V}_f{}^+$) of case H7. Contour levels of $\tilde{U}_f{}^+$, $\tilde{V}_f{}^+ =$ 0.1 and −0.1 are marked by red and magenta curves. The phase-averaged sediment-bed height, $\tilde{H}_b$, is shown by the dashed curve. The vertical thin lines indicate the locations where wall-normal profiles of each quantity are extracted. (*b*) The corresponding phase-averaged particle velocity components ($\tilde{U}_p{}^+$, $\tilde{V}_p{}^+$). (*c*) Values of $\tilde{U}_f$ and $\tilde{U}_p$ extracted along the fluid–bed interface (shown by the curve at the top of the figure). The red dashed line represents the mean ripple migration velocity. (*d*) Same as panel (*c*) but for $\tilde{V}_f$ and $\tilde{V}_p$. (*e*) Wall-normal profiles $\tilde{U}_f$ and $\tilde{U}_p$ at selected streamwise locations. Profiles are, from left to right, at $\tilde{x}/D = 0$, 30 and 112 consecutively. The horizontal dashed lines indicate the location of the fluid–bed interface at the corresponding streamwise locations. (*f*) Same as panel (*e*) but for $\tilde{V}_f$ and $\tilde{V}_p$.

in figure 4(*a*). Let us remark that a zero-valued contour level does not precisely demarcate the extent of the re-circulation region as there is very small but non-zero mean velocity inside the bed. The value of $\tilde{U}_f$ gradually increases along the ripple stoss side up to the crest. Similarly, in the outer flow region, $\tilde{U}_f$ exhibits higher velocity values in the flow contraction region above the crest and lower velocity values in the expansion region above the ripple stoss side. The wall-normal fluid velocity also exhibits an upward moving fluid region ($\tilde{V}_f > 0$) above the stoss side and a downward moving fluid region ($\tilde{V}_f < 0$) above the region downstream of the crest. A small region of positive $\tilde{V}_f$ is observed immediately downstream of the crest in the vicinity of the fluid–bed interface that corresponds to the up-lifting fluid of the re-circulation region. As y tends to the upper boundary, $\tilde{V}_f$ tends to zero due to the imposed boundary condition.

The mean particle velocities also exhibit generally the same spatial structure as that of the fluid. From the intensity of the colour plots, it can be seen that the magnitude of streamwise particle velocity is on average smaller than that of the fluid in the region far above the fluid–bed interface, except in the re-circulation region. The opposite is true for the wall-normal component $\tilde{V}_p$, which is observed to be higher in magnitude than that of the fluid. More quantitative comparison of the fluid and particle velocities can be inferred from the profiles along the location of the fluid–bed interface shown in figure 4(c,d) as well as from the wall-normal profiles of the same quantities at selected streamwise locations $\tilde{x}/D = 0$ (near crest), $\tilde{x}/D = 30$ (in trough) and $\tilde{x}/D = 112$ (on the stoss side of the ripple) shown in figure 4(e,f). It can be seen that the fluid/particle velocities strongly vary along the fluid–bed interface. Note that the fluid–bed interface is permeable and is subject to active mass and momentum exchange of both phases as a result of erosion, transport and deposition of sediment particles as well as the fluid motion therein. At the ripple crest the streamwise velocity of both phases reaches local maximum values of up to $\tilde{U}_f{}^{+} \approx 4$ and $\tilde{U}_p{}^{+} \approx 3$, whereas in the ripple troughs, velocities decrease considerably, attaining negative values in the re-circulation region. Further observation is that particles are on average moving at a smaller streamwise velocity than that of the fluid along the fluid–bed interface, except in the re-circulation region, where the opposite trend is observed. On the stoss side of the ripples, the value of the velocity lag between the two phases ranges between $1u_\tau$ and $1.5u_\tau$, whereas in the re-circulation region, a negative velocity lag of up to $-0.35u_\tau$ is observed. The origin of the velocity lag could be explained by the combined effect of the preferential distribution of inertial particles with respect to the near-wall high- and low-speed fluid regions (Kidanemariam *et al.* 2013) and the fact that finite-sized particles feel the traction effect of neighbouring particles, which are located at a lower wall-normal location and are moving at a lower velocity, more than fluid particles do. Note that the particle velocity is much higher than the mean ripple migration velocity u_D over the entire stoss side of the ripples, while the opposite is true at locations downstream of the crest. This observation is in line with the fact that ripples propagate as a result of erosion and deposition of sediment grains at the bed surface. $\tilde{V}_f$ and $\tilde{V}_p$ along the fluid–bed interface exhibit a notably different trend when compared with their streamwise counterparts. On the stoss side, $\tilde{V}_f$ and $\tilde{V}_p$ are positive while the difference between their values is not substantial. Moreover, the location of the local maximum of $\tilde{V}_f$ ($\tilde{V}_p$) is observed to be located further upstream of the crest when compared with the streamwise components. Both phases exhibit an approximately zero value of the wall-normal velocity in the vicinity of the crest.

The wall-normal profiles of fluid and particle velocities presented in figure 4(e,f) further corroborate the above observations. Note that the apparent velocity lag is significant even at wall-normal locations well above the fluid–bed interface. Namely, positive velocity lag on the stoss side of the ripples ($\tilde{U}_f > \tilde{U}_p$) and negative velocity lag in the re-circulation region ($\tilde{U}_f < \tilde{U}_p$). In the region well above the fluid–bed interface, the preferential sampling of low-speed fluid regions by inertial particles (Kidanemariam *et al.* 2013) is expected to be the dominant reason for the observed positive velocity lag. The negative velocity lag in the re-circulation region is again attributed to particle inertia. Sediment particles that are suspended from the crest with high momentum into the re-circulation

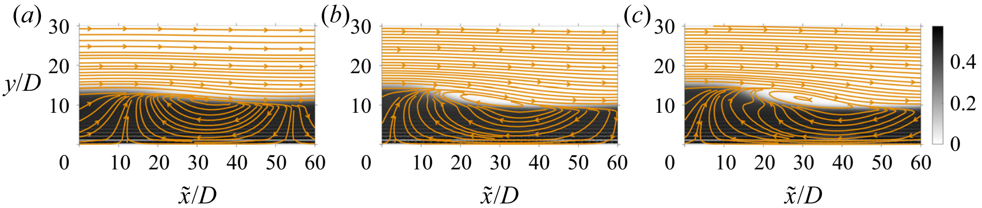

Figure 5. Streamlines of the phase-averaged fluid velocity (close-up in the region downstream of the ripple crests). The grey-scale plot in the background represents the mean solid volume fraction $\tilde{\phi}_p$. (*a*), H4; (*b*), H6; (*c*), H7.

region do not immediately adapt to the new environment, thus resulting in a statistically higher mean particle velocity than that of the fluid. Turning to the wall-normal velocity component, the profiles further highlight the mean positive and negative velocities upstream and downstream of ripple crests, respectively. Furthermore, upstream of the crest and above the fluid–bed interface, the particles' wall-normal velocity is observed to be larger in magnitude than that of the fluid whereas downstream of the crest and above the fluid–bed interface, the particle velocity is observed to be substantially smaller (larger in absolute value) than that of the fluid. This latter effect is in part attributed to the effect of gravity on the suspended sediment grains that settle in the re-circulation region.

Finally, we remark that the corresponding results for cases H4 and H6 are in general of similar spatial structure and plots are not included. In figure 5 we report the streamline plot of the mean flow for the three cases. The plots effectively show the development of the re-circulation region at different stages of the ripple evolution. Incidentally, the streamlines also show the structure of the minute flow inside the sediment bed. The overall trend of the spatial variation of the mean streamwise and wall-normal components of the fluid velocity is consistent with the experiments by Charru & Franklin (2012) of the flow over barchan dunes. However, a rigorous analysis of the structure of the mean flow and turbulent statistics of the fluid and particle phases, as well as comparison with available experiments, is left for future work.

4.2. *Total shear stress and its spatial variation along the interface*

As has been reported in KU2017, the driving mean pressure gradient in the flow is balanced by the sum of the fluid shear stress and stress contribution from the fluid–particle interaction resulting in a linearly varying plane-averaged total shear stress across the depth of the channel. This linearity can also be recovered from the phase-averaged statistics. In the two-dimensional flow evolving over the ripples, the total plane-averaged fluid shear stress comprises the viscous and turbulent Reynolds stresses as well as contribution from the ripple form-induced dispersive stress (Raupach & Shaw 1982; Nikora *et al.* 2007*a*). Similarly, the Eulerian particle–fluid interaction contribution (the last term in 5.10 in Kidanemariam & Uhlmann 2017) could in principle be recovered from its phase-shifted counterpart $\langle \tilde{f}_x \rangle_{zt}$. However, the latter quantity is not explicitly available for evaluation because we have only accumulated time history of the Lagrangian hydrodynamic ($\boldsymbol{F}_p^{H(l)}$) and collision ($\boldsymbol{F}_p^{C(l)}$) forces for each particle l by integrating over the particle surface. As has been demonstrated by Uhlmann (2008), the mean Eulerian force density can be

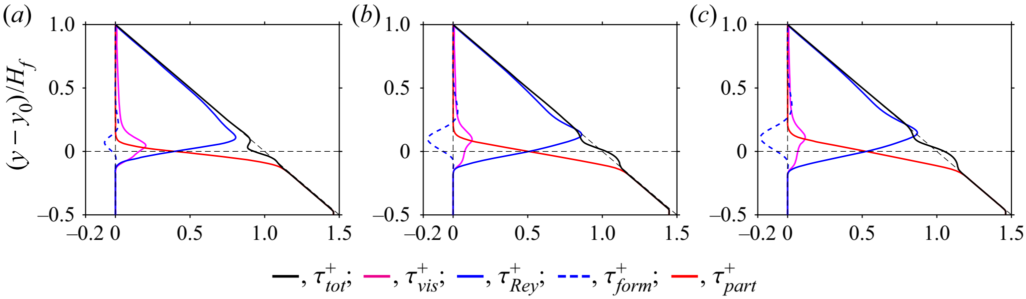

Figure 6. Wall-normal profiles of the different contributions to the plane-averaged total shear stress computed based on the phase-shifted statistics (4.2): (*a*) H4; (*b*) H6; (*c*) H7.

approximated from the total hydrodynamic force acting on the particles, *viz.*

$$\langle \tilde{f} \rangle_{zt} \approx -\langle \tilde{f}^H_p \rangle_{zt} \tilde{\phi}_p / V_p, \tag{4.1}$$

where the field f^H_p is computed from $F^{H(l)}_p$ using relation (B5) in Appendix B and $V_p \equiv \pi D^3/6$ is the volume of a single spherical particle. Here, $\tilde{\phi}_p$ is the mean solid volume fraction defined in (B12). The error of this approximation is expected to be small as long as there is no sharp local gradient in $\tilde{\phi}_p$. Thus, the total plane-averaged shear stress is given by

$$\tau_{tot} = \underbrace{\rho_f \nu \partial_y \langle \tilde{u}_f \rangle_{xzt}}_{\tau_{\mathrm{vis}} = \rho_f \nu \partial_y U_f} - \underbrace{\left(\underbrace{\rho_f \langle \tilde{u}'_f \tilde{v}'_f \rangle_{xzt}}_{\tau_{Rey}} + \underbrace{\rho_f \langle \langle \tilde{u}''_f \tilde{v}''_f \rangle_{zt} \rangle_x}_{\tau_{form}} \right)}_{= \rho_f \langle u'_f v'_f \rangle_{xzt}} - \underbrace{\frac{1}{V_p} \int_y^{L_y} \langle \langle \tilde{f}^H_{p,x} \rangle_{zt} \tilde{\phi}_p \rangle_x \, \mathrm{d}y}_{\tau_{part} = \int_y^{L_y} \langle f_x \rangle \, \mathrm{d}y} . \tag{4.2}$$

Definitions of the velocity fluctuation covariances $\langle \tilde{u}'_f \tilde{v}'_f \rangle_{xzt}$ and $\langle \tilde{u}''_f \tilde{v}''_f \rangle_{zt}$ are given in Appendix B. Figure 6 shows the wall-normal profiles of the different contributions in (4.2). It can be seen that the actual total shear stress is sufficiently recovered with this approach. A slight deviation from the linear variation is observable, in regions where the above introduced errors are expected to be non-negligible (in the vicinity of the fluid–bed interface location). We remark that for the purpose of verifying the convergence of statistics we actually evaluate the forcing term $\langle f_x \rangle_{xzt}$ during run time. As shown in Appendix C, τ_{tot} is indeed varying linearly throughout the channel height. Moreover, figure 6 shows that the form-induced stress contribution is of opposite sign to that of the turbulent Reynolds stress, except in the outer fluid region where it exhibits small positive values and subsequently tends to zero for increasing y. This means that there is high momentum fluid that is carried away from the bottom into the outer flow and *vice versa* as a result of the form-induced stress. However, the magnitude of the form-induced stress is small when compared with that of the Reynolds stress. The form-induced momentum transfer is explainable by observing the streamlines of the mean flow. Upstream of the crest, the mean flow increases in the positive streamwise direction and is characterised by a positive wall-normal velocity (first quadrant stress), while downstream of the crest, the flow decreases and is downward moving (third quadrant stress).

The analysis presented above provides an integral information on the total shear stress of the flow over a space and time varying sediment bed. However, it fails to provide

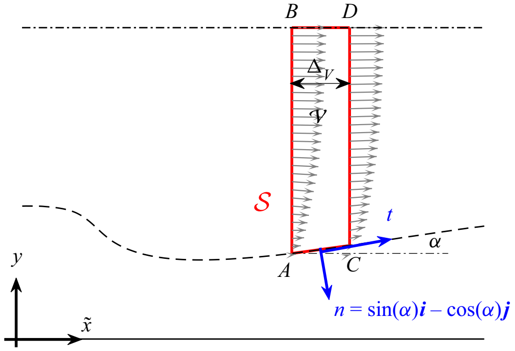

Figure 7. A control volume $\mathcal{V}$ (with unit spanwise extent), enclosed by a surface $\mathcal{S}$ over which the momentum equation is integrated for the determination of the boundary shear stress. $\mathcal{V}$ is moving at the constant mean ripple velocity u_D in the positive streamwise direction. Note that $\mathcal{V}$ is a quadrilateral, i.e. the edge AC is a straight line with a slope $\tan(\alpha)$. Here, $\boldsymbol{n}$ and $\boldsymbol{t}$ are the unit normal and tangential vectors at the edge AC, respectively and $\boldsymbol{i}$ and $\boldsymbol{j}$ are the unit vectors in the $\tilde{x}$ and y directions, respectively.

information on the local boundary shear stress and its spatial variation with respect to the evolving bed. This quantity, and its relation to the local sediment flow rate, is highly relevant in sediment transport modelling and thus its accurate determination is important. In developed bedforms, the total boundary shear stress is the sum of the dune-form drag that results from the pressure difference between the regions upstream and downstream of the crest of a ripple, as well as the skin friction due to fluid viscous stress and fluid–particle interaction at the grain scale (see e.g. Yalin 1977; Nikora *et al.* 2007*a*). Usually in experiments, the form drag is estimated by integration of pressure measurements along a stationary bedform and the skin friction is estimated by assuming a logarithmic velocity profile below the lowest velocity measurement point and performing extrapolation in which a certain value for the hydrodynamic roughness height has to be prescribed (see e.g. McLean & Smith 1986; Maddux, Mclean & Nelson 2003; Nikora *et al.* 2007*b*). Similarly, Charru & Franklin (2012) estimate the boundary stress by extrapolation of the total shear-stress profile (corrected for streamline curvature) within the internal developing boundary layer to the surface of the bed. However, the degree of uncertainty inherent in such approaches is substantial, and in the present case, proved to be unreliable due to the strong degree of particle modulation therein. Instead, we have determined the local boundary shear stress by evaluating the momentum balance in a local control volume as described below.

First, we define quadrilateral control volumes $\mathcal{V}$ with a fixed shape and of unit spanwise extent, enclosed by a surface $\mathcal{S}$, an exemplary one of which is shown in figure 7. Here, $\mathcal{V}$ is moving at the constant mean ripple velocity u_D in the positive streamwise direction and is demarcated by the locations of the points A, B, C and D. The top boundary (face BD) coincides with the top boundary of the computational domain while faces AB and CD are aligned perpendicular to the streamwise direction. The streamwise extent of the control volume is chosen to be two particle diameters (i.e. $\Delta_V = 2D$) so that the ripple geometry is sufficiently resolved. Points A and C coincide with the fluid–bed interface. The small interface curvature between A and C is ignored and thus face AC is a straight line segment of constant slope $\tan(\alpha)$. Let us recall that the fluid–bed interface is defined based purely on a threshold of the solid volume fraction and in general is not exactly aligned with the streamlines of the mean flow. It is expected that there would be advective momentum transfer across face AC as a result of the mean fluid/particle flux across it.

The Reynolds phase-averaged momentum equation, integrated over $\mathcal{V}$ can be written as

$$\oint_{\mathcal{S}} (\tilde{\boldsymbol{U}}_f \tilde{\boldsymbol{U}}_f) \boldsymbol{\cdot} \boldsymbol{n}\, \mathrm{d}S + \oint_{\mathcal{S}} \left(\langle \tilde{\boldsymbol{u}}'_f \tilde{\boldsymbol{u}}'_f \rangle_{zt} + \frac{1}{\rho_f} \langle \tilde{p} \rangle_{zt} \bar{\bar{\boldsymbol{I}}} - \langle \tilde{\bar{\bar{\boldsymbol{\tau}}}} \rangle_{zt} \right) \boldsymbol{\cdot} \boldsymbol{n}\, \mathrm{d}S - \int_{\mathcal{V}} \langle \tilde{\boldsymbol{f}} \rangle_{zt}\, \mathrm{d}V = \int_{\mathcal{V}} \langle \varPi \rangle_t\, \mathrm{d}V, \tag{4.3}$$

where $\langle \tilde{p} \rangle_{zt} \bar{\bar{\boldsymbol{I}}}$ and $\langle \tilde{\bar{\bar{\boldsymbol{\tau}}}} \rangle_{zt}$ are the phase-averaged pressure and fluid shear-stress tensor, respectively. Also, $\langle \varPi \rangle_t$ is the driving pressure gradient term averaged in the steady ripple propagation interval. Note that the time rate-of-change term of the momentum equation vanishes in the moving frame of reference in the steady ripple propagation interval. We are interested in determining the total shear stress at the bottom face AC by integrating the momentum balance (4.3) over $\mathcal{V}$. The total shear force acting on face AC has contributions both from the fluid stresses as well as the particle–fluid interactions

$$\tilde{\boldsymbol{R}} = \int_{AC} (\langle \tilde{\bar{\bar{\boldsymbol{\tau}}}} \rangle_{zt} - \langle \tilde{\boldsymbol{u}}'_f \tilde{\boldsymbol{u}}'_f \rangle_{zt}) \boldsymbol{\cdot} \boldsymbol{n}\, \mathrm{d}S + \int_{\mathcal{V}} \langle \tilde{\boldsymbol{f}} \rangle_{zt}\, \mathrm{d}V, \tag{4.4}$$

and the average total boundary shear stress $\tilde{\tau}_b$ (per unit spanwise width) is then equal to the component of $\tilde{\boldsymbol{R}}$ parallel to AC, divided by the length of the segment AC ($\varDelta_V \cos\alpha$) *viz.*

$$\tilde{\tau}_b = \frac{1}{\varDelta_V \cos\alpha} (\tilde{\boldsymbol{R}} - (\tilde{\boldsymbol{R}} \boldsymbol{\cdot} \boldsymbol{n})\boldsymbol{n}) \boldsymbol{\cdot} \boldsymbol{t}. \tag{4.5}$$

Here, $\boldsymbol{n} = \sin(\alpha)\boldsymbol{i} - \cos(\alpha)\boldsymbol{j}$ is the unit normal perpendicular to the interface while $\boldsymbol{t}$ is the corresponding tangential unit vector; $\boldsymbol{i}$ and $\boldsymbol{j}$ are the unit vectors aligned in the positive streamwise and wall-normal directions, respectively (cf. schematics in figure 7). The fluid–solid interaction term in (4.4) implicitly accounts for the total stress as a result of all particles within the control volume, whether moving as bedload or suspended.

The value of $\tilde{\tau}_b$ can be computed either by directly evaluating (4.5), or from the balance (4.3) where each term is integrated over the volume $\mathcal{V}$ and all bounding faces (assuming statistical stationarity). In practice, we have resorted to the latter approach as approximating the fluid–particle interaction term from the available integral Lagrangian particle forces introduces non-negligible errors in regions of sharp solid volume fraction gradients at the location of face AC (see discussion above). Moreover, especially in experiments, the fluid–solid interaction term is not easily accessible. Thus the approach chosen here at the same time demonstrates a procedure for accurately retrieving the boundary shear stress from experimentally measurable quantities.

Figure 8(*a*) shows the streamwise variation of the boundary shear stress $\tilde{\tau}_b$ along the fluid–bed interface, computed with the above-described method. Profiles of $\tilde{\tau}_b$ for all cases are seen to exhibit a similar evolution along the ripple geometry: a sharp decrease downstream of the crest attaining negative values beneath the re-circulation region, with the location of the minimum value in the range $\tilde{x} \approx 0.14\lambda$–$0.16\lambda$, followed by a sharp increase in the following region up to $\tilde{x} \approx 0.45\lambda$. Subsequently, $\tilde{\tau}_b$ exhibits a quasi-plateau region with mild increase up to the location of the maximum at $\tilde{x} \approx 0.85\lambda$ followed by a mild decrease region in the interval 0.85λ up to the location of the crest. The location of the minimum $\tilde{\tau}_b$ is observed to be upstream of the bed's trough while that of the maximum of $\tilde{\tau}_b$ is upstream of the ripple crest (with a shift of approximately $15D$, $23D$ and $27D$ for cases H4, H6 and H7). The observed negative boundary shear stress downstream of the crest is expected due to the reversed flow in the re-circulation region. Note that, in correspondence to the almost non-existent re-circulation region of case H4 (cf. the

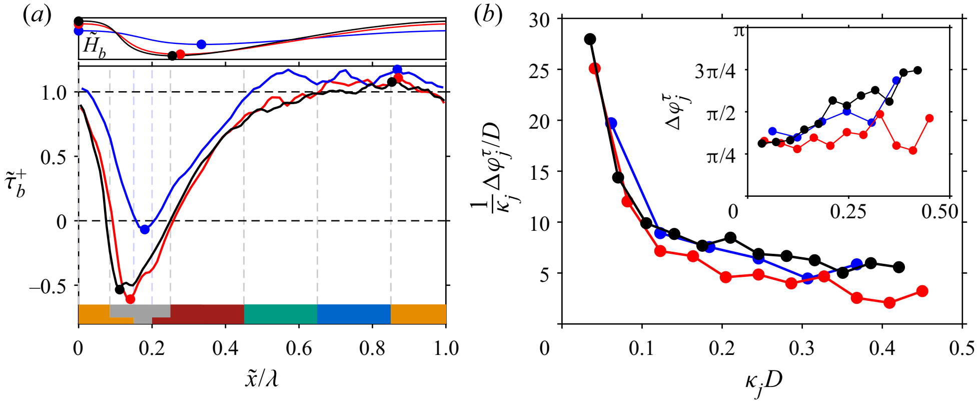

Figure 8. (*a*) Streamwise variation of the boundary shear stress $\tilde{\tau}_b/(\rho_f u_\tau^2)$: blue line, H4; red line, H6; black line, H7. The global minima and maxima of $\tilde{\tau}_b$ are marked by the dot symbols. The mean ripple profile of each of the cases, along with the location of the crest (maximum of $\tilde{H}_b$) and trough (minimum of $\tilde{H}_b$) are shown at the top of the panel for reference. The colour code at the bottom of the panel and the corresponding vertical dashed lines demarcate different regions of the $\tilde{\tau}_b$ profile, and it is later used in colour coding the data points in figure 12 (for instance, the grey region shows the region where $\tilde{\tau}_b$ attains negative values). (*b*) Upstream phase shift, normalised by the particle diameter, of the first few dominant Fourier modes of $\tilde{\tau}_b$ relative to the phase of the corresponding modes of $\tilde{H}_b$ for the different cases (H4, —●—, blue; H6, —●—, red; H7, —●—, black). The inset shows the phase shift in radians.

streamline plots in figure 5), the region where $\tilde{\tau}_b$ of case H4 attains a negative value is very small. The observed shift of the maximum of $\tilde{\tau}_b$ with respect to the ripple crest, which is a consequence of the fluid inertia, is also in line with previous literature on flow over undulating boundaries (Benjamin 1959; Jackson & Hunt 1975; Zilker & Hanratty 1979; Charru *et al.* 2013). The variation of $\tilde{\tau}_b$ along the stoss side of the ripple is comparable to those reported by Charru & Franklin (2012) for the flow over evolving barchan dunes, although those authors report the maximum of the shear stress to be located at the brink of the barchan, contrary to our findings. However, we remark that the variation between the maximum value of $\tilde{\tau}_b$ and the value at the crest is fairly small and is therefore difficult to capture subject to measurement and extrapolation technique uncertainties. We also remark that, in Charru & Franklin (2012), the reported boundary shear stress is normalised by the unperturbed smooth wall friction velocity upstream of the barchan dune and thus the normalised values of $\tilde{\tau}_b$ are larger in magnitude when directly compared with our numerical data.

The shift of the extrema with respect to the ripple geometry discussed above does not provide a complete picture of the phase shift between the shear stress and topography, since the shapes of $\tilde{\tau}_b$ and $\tilde{H}_b$ curves differ visibly. Nevertheless, since $\tilde{\tau}_b$ and $\tilde{H}_b$ are periodic, a more robust 'average' phase shift can be estimated from the separation length at which the cross-correlation between the two has a maximum value. The average phase shift, computed by the latter method, reads approximately $16D$, $18D$ and $19D$ for cases H4, H6 and H7 (cf. table 3). That is, the shear stress is in advance of the topography by approximately 16–19 particle diameters for all simulated cases, showing only few particle diameters of variation (in contrast to the observation regarding the locations of the maxima). Note that, due to the nonlinear nature of the system, the reported phase shift is an integral quantity and does not reflect the phase shift of the individual modes. To this end, we have computed the phase shift of the Fourier modes of $\tilde{\tau}_b$ relative to the phase of the corresponding modes of $\tilde{H}_b$. More precisely, the phases of $\tilde{\tau}_b$ and $\tilde{H}_b$ are computed

Case	H4	H6	H7
$\bar{\varphi}_{\tilde{\tau}_d\tilde{H}_b}/D$	15.7	17.9	18.9
$\bar{\varphi}_{\tilde{\tau}_d\tilde{q}_p}/D$	17.6	18.5	19.3

Table 3. Average phase advance in particle diameters of the boundary shear stress with respect to the ripple profile, $\bar{\varphi}_{\tilde{\tau}_d\tilde{H}_b}$, and with respect to the particle flow rate, $\bar{\varphi}_{\tilde{\tau}_d\tilde{q}_p}$. The values are computed from the separations at which the $\tilde{\tau}_b$–$\tilde{H}_b$ and $\tilde{\tau}_b$–$\langle\tilde{q}_p\rangle_{zt}$ cross-correlation functions are maximum, respectively.

based upon the real and imaginary parts of their respective Fourier coefficients and subsequently a relative phase shift $\Delta\varphi_j$ for mode j is defined as the difference between the two. Figure 8(*b*) shows the mode-wise phase shift as a function of the wavenumber κ_j of the first few significant Fourier modes. Interestingly, a dispersion among the different modes can be observed, $\Delta\varphi_j/\kappa_j$ exhibiting a decreasing trend with decreasing wavelength ($\Delta\varphi_j$ in radians shows the opposite trend, largest wavelength associated with smallest phase shift and *vice versa*). A further observation is that the phase-shift dispersion collapses fairly well for the three cases only being limited at the lower κ end of the spectrum by the discreteness of the available numerical harmonics. This indicates that the phase shift depends purely on the imposed flow conditions and not on the state of the ripple evolution. The above findings corroborate previous works (Fourrière *et al.* 2010; Claudin, Charru & Andreotti 2011) that typically consider a single mode in their modelling efforts. The phase shift between the local boundary shear stress and the sediment-bed height is believed to be the main factor for destabilising a mobile sediment bed during the initial stages of ripple formation as well as during the subsequent nonlinear evolution process (Andreotti & Claudin 2013; Charru *et al.* 2013).

Another way of looking at the phase advance of the shear stress is to distinguish between its component that is in quadrature and the one that is in phase with respect to the bed topology. In theoretical analysis, a sinusoidal bottom perturbation of small amplitude is usually considered. Then the flow over a bottom perturbation is analysed as a layered structure: an outer inertia dominated region in balance with the form-induced pressure gradient and where viscous effects are less important and an inner logarithmic region close to the boundary. The matching between these two in some intermediate region results in the phase advance of the shear stress with respect to the bottom undulation, the shear-stress maximum being located upstream of the crest (Charru *et al.* 2013). To understand the physical mechanisms, the Fourier coefficients $\hat{\tau}_j$ of the boundary shear stress $\tilde{\tau}_b$ are commonly expressed in terms of two hydrodynamical parameters $\mathcal{A}$ and $\mathcal{B}$ as (Charru *et al.* 2013; Duran Vinent *et al.* 2019)

$$\hat{\tau}_j^+ \exp(-\mathrm{i}\varphi_{b,j}) = \kappa_j|\hat{A}_j|(\mathcal{A}_j + \mathrm{i}\mathcal{B}_j), \tag{4.6}$$

where $\hat{A}_j$ are the corresponding Fourier coefficients of the ripple morphology, $\varphi_{b,j}$ is the phase shift of mode j and where $\mathrm{i} \equiv \sqrt{-1}$ is the imaginary unit. Note that, in the linear analysis, a single sinusoidal mode (with zero phase shift) is considered for the bottom perturbation. In our case, the interaction between the flow and the self-formed finite-size, asymmetric ripples is far from linear. The ripple morphology consists of a band of modes each with distinct phase shift $\varphi_{b,j}$. Fuller understanding requires rigorous analysis of the broadband modulation that is beyond the scope of the paper. Nevertheless, it is worthwhile to look at our data in the context of the linear theories that have been the basis for modelling sediment-bed evolution. Thus, $\hat{\tau}_j$ is multiplied by $\exp(-\mathrm{i}\varphi_{b,j})$.

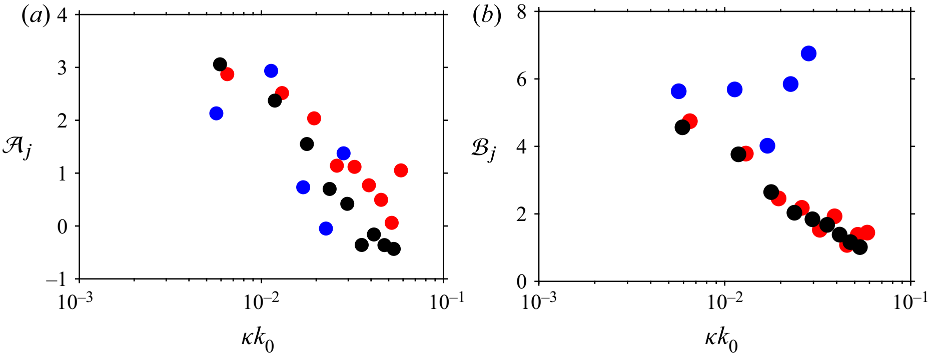

Figure 9. (*a*) The symmetric real component $\mathcal{A}$ and (*b*) the anti-symmetric imaginary component $\mathcal{B}$ of the first few modes of the bottom shear stress (relative to the phase of the corresponding modes of the ripple morphology): blue circles, H4; red circles, H6; black circles, H7.

The parameters $\mathcal{A}$ and $\mathcal{B}$ exhibit different spatial structures and different physical meanings. In the linear regime, $\mathcal{A}$ is in-phase (symmetric) while $\mathcal{B}$ is in-quadrature (anti-symmetric) with respect to the bottom surface. A positive value of $\mathcal{B}$ is associated with particle erosion from the trough and deposition at crest while a positive value of $\mathcal{A}$ is associated with downstream migration of the perturbation (Charru *et al.* 2013). Figure 9 shows the shear-stress components $\mathcal{A}$ and $\mathcal{B}$ corresponding to the first few modes extracted from the DNS data as a function of the wavenumber scaled with the hydrodynamic roughness k_0 (cf. § 3). The data points collapse well for the three cases (except for the scatter in the data of case H4), corroborating our previous argument that the phase shift of individual modes is independent of the ripple evolution stage. Compared with theoretical linear predictions, the values of $\mathcal{A}$ and $\mathcal{B}$ fall in general within the same order of magnitude (Fourrière *et al.* 2010; Charru *et al.* 2013; Duran Vinent *et al.* 2019). However, we recall that the hydrodynamic roughness height k_0, which is an important ingredient of the above models, is inferred from the flow over stationary roughness. Moreover, the flow separation downstream of the ripple crests is known to alter the shear-stress phase advance (Charru *et al.* 2013). Therefore, a direct comparison of the data presented in figure 9 with the theoretical linear predictions is not meaningful.

4.3. *Relationship between the local sediment flux and the boundary shear stress*

The phase-averaged total sediment flow rate per unit width can be evaluated from the phase-averaged particle statistics as

$$\langle \tilde{q}_p \rangle_{zt}(x) = \int_0^{L_y} \langle \tilde{q}^{2D}_{p,x} \rangle_{zt} \, \mathrm{d}y, \tag{4.7}$$

where $\langle \tilde{q}^{2D}_{p,x} \rangle_{zt} \equiv \tilde{U}_p \tilde{\phi}_p$ is the streamwise component of the phase-averaged two-dimensional particle flow rate per unit area. Note that $\langle \tilde{q}_p \rangle_{zt}$ incorporates all particle transport modes, bedload and suspended load. Figure 10(*a*) shows the streamwise variation of $\langle \tilde{q}_p \rangle_{zt}$. The values of $\langle \tilde{q}_p \rangle_{zt}$ are different among the cases, that of case H7 being the largest while that of case H4 being the smallest for most of the ripple profile, including the stoss side. This is expected due to the difference in the average bottom friction among the cases that is proportional to the ripple height (see the bottom friction evolution in figure 2). However, in the region $0.1\lambda \lesssim \tilde{x} \lesssim 0.35\lambda$, the opposite trend is observed, i.e.

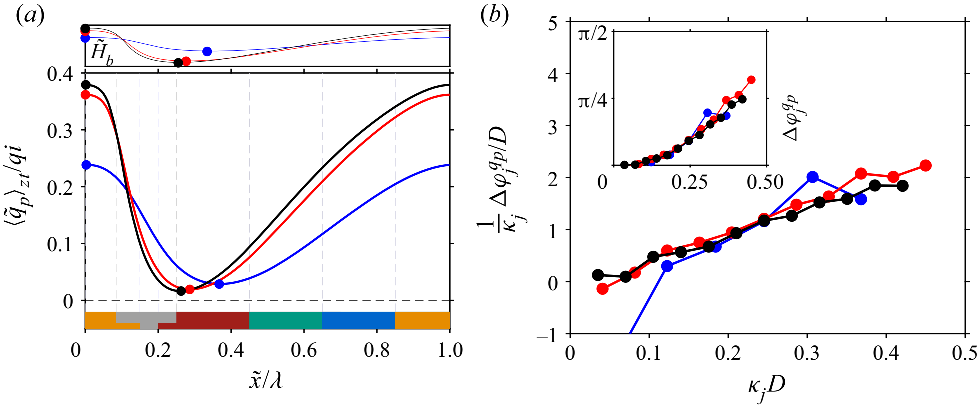

Figure 10. Streamwise variation of the volumetric particle flow rate $\langle \tilde{q}_p \rangle_{zt}$, normalised by the inertial scale $q_i = U_g D$. The global minima and maxima are marked by the dot symbols. The mean ripple profile of each of the cases, along with the location of the crest (maximum of $\tilde{H}_b$) and trough (minimum of $\tilde{H}_b$) are shown at the top of the panel. (*b*) Upstream phase shift, normalised by particle diameter, of the first few dominant Fourier modes of $\langle \tilde{q}_p \rangle_{zt}$ relative to the phase of the corresponding modes of $\tilde{H}_b$ for the different cases. The inset shows the phase shift in radians. Colour coding is the same as for figure 8.

$\langle \tilde{q}_p \rangle_{zt}$ of H4 is the largest. This can be explained by a combined effect of particle inertia and hindrance related to the smaller ripple amplitude and the very mild recirculation (the boundary layer of case H4 is not as disrupted as that of the other cases). For all cases, the particle flow rate exhibits a minimum value in the location very close to the trough and a maximum value very near the crest essentially in phase with the ripple geometry. Such an in-phase variation of the ripple morphology and the sediment flux is a consequence of mass conservation (under the condition that the bedforms are steadily migrating and are of constant shape) as described by the Exner equation (Charru *et al.* 2013). However, a closer look into the spectral decomposition of the phase shift (figure 10*b*) reveals that, although the dominant modes have essentially zero phase shift, there is a clear trend of (somewhat linear) phase-shift increase with increasing wavenumber, albeit only to within two particle diameters. The mode-wise resolved phase shift will be discussed in more detail below in relation to that of the bottom shear stress. In table 3 we report the average phase shift between $\tilde{\tau}_b$ and $\langle \tilde{q}_p \rangle_{zt}$ that measures approximately 18–19 particle diameters, fairly independent of the ripple dimension.

A key quantity in sediment transport modelling is the local relationship between $\tilde{\tau}_b$ and $\langle \tilde{q}_p \rangle_{zt}$. It has been a common practice to relate the two through algebraic semi-empirical formulae (e.g. Meyer-Peter & Müller 1948; Wong & Parker 2006) that are popular in engineering applications. However, it is recognised that the sediment flux does not immediately adapt to local change in the shear stress (Sauermann *et al.* 2001; Charru 2006; Fourrière *et al.* 2010; Claudin *et al.* 2011). Models such as that by Meyer-Peter & Müller (1948) do not incorporate such a relaxation effect and thus have been shown to be not adequate to predict the spatial structure of the particle flow rate, in particular in the context of bedform formation and evolution. Comparing figures 8(*a*) and 10(*a*) it is evident that the two profiles do not follow the same trend, corroborating the relevance of a relaxation process. It is noteworthy that the location of the respective maxima/minima do not fall at the same location. Moreover, $\langle \tilde{q}_p \rangle_{zt}$ is observed to be entirely of positive value across the entire ripple profile, including in the re-circulation region where $\tilde{\tau}_b$ is negative, for all cases. This shows that the spatial structure of sediment transport

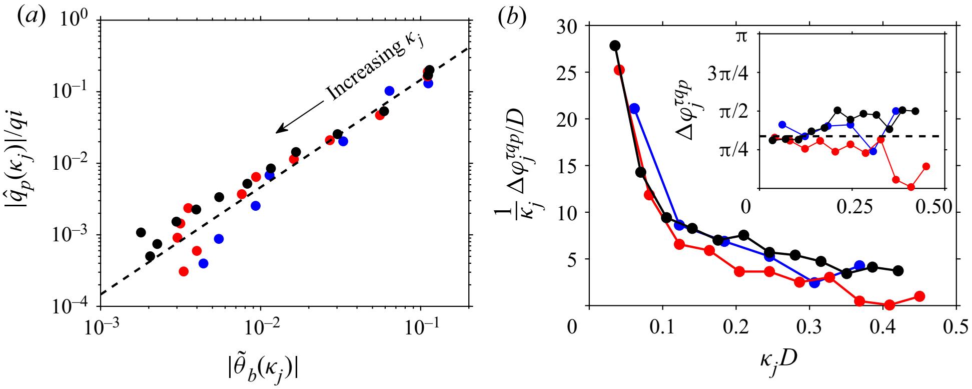

Figure 11. (*a*) Amplitude of the Fourier coefficients of the first few modes of $\langle\tilde{q}_p\rangle_{zt}$ as a function of the corresponding amplitudes of non-dimensional local Shields number. The dashed line is a power-law function given by $|\hat{q}_p|/q_i = 4.63|\hat{\theta}_b|^{1.5}$ that best fits the data: blue circles, H4; red circles, H6; black circles, H7. (*b*) Upstream phase shift of the boundary shear stress relative to the phase of particle flow rate. The dashed line shows an average phase shift of the dominant modes (averaged over all cases). Colour coding is the same as for figure 8.

cannot be entirely predicted by classical models where the particle flow rate is expressed in terms of local bottom shear stress alone. The non-local correlation between $\tilde{\tau}_b$ and $\langle\tilde{q}_p\rangle_{zt}$ can be scrutinised by analysing the amplitude and phase shift of the corresponding Fourier modes. Figure 11(*a*) presents the amplitude of the first few dominant Fourier coefficients of $\langle\tilde{q}_p\rangle_{zt}$ (normalised by the inertial scaling $q_i = U_g D$) as a function of the corresponding amplitude of the bottom shear-stress coefficients (expressed in terms of the non-dimensional local Shields number $\tilde{\theta}_b = \tilde{\tau}_b/((\rho_p - \rho_f)gD)$), while figure 11(*b*) shows the mode-wise phase shift between the two quantities (both in particle diameters and in radians). Interestingly, the correlation of the amplitudes for all cases sufficiently collapses and it is well represented by a power-law fit of the form

$$|\hat{q}_p|/q_i = \alpha|\hat{\theta}_b|^{\beta}, \tag{4.8}$$

with fit parameters $\alpha = 4.63$ and $\beta = 1.5$. The phase shift in radians seems to exhibit no particular trend and is fairly independent of the wavenumber, in particular at the lower wavenumber end of the spectrum (subject to the scatter of the data). For our considered data point, the average phase shift reads $\Delta\varphi_{av} \approx 0.336\pi$ (the dashed line in that figure). This translates to a wavenumber-dependent phase shift in particle diameters $\Delta\varphi_j/D = \Delta\varphi_{av}/(\kappa_j D) \approx 27/\kappa_j$. The above observation motivates us to write a simplified relationship between the bottom shear stress and particle flow rate, which incorporates the phase shift between the two, as follows:

$$q_p = \sum_{j=0}^{modes} \alpha|\hat{\theta}_b|^{\beta-1}\hat{\theta}_b \exp(-\mathrm{i}\Delta\varphi_{\mathrm{av}}) \exp(\mathrm{i}\kappa_j\tilde{x}), \tag{4.9}$$

where φ_{av} is the average mode-wise phase shift for modes $j > 0$ (there cannot be a phase shift in the zeroth-mode). We remark that (4.9) is obtained from a fit to the $\langle\tilde{q}_p\rangle_{zt}$–$\tilde{\theta}_b$ relationship that has resulted from a nonlinear process. Moreover, an average phase shift (in radians) is considered that ignores possible mode-wise dispersion. However, it can be argued that inclusion of the phase shift between the shear stress and sediment flux that

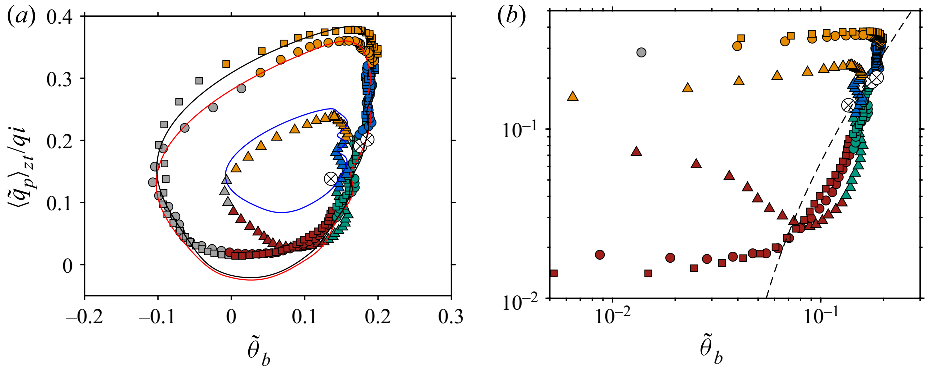

Figure 12. (*a*) Particle flow rate $\langle \tilde{q}_p \rangle_{zt}$ as a function of the local phase-averaged Shields number $\tilde{\theta}$: $\triangle$, H4; $\circ$, H6; $\square$, H7. Marker colours indicate the different locations along the ripple profile (cf. colour coding in figure 8). The space- and time-averaged mean particle flow rate $\langle q_p \rangle_{zxt}$ for the three cases are shown by the symbols $\otimes$. The solid curves correspond to the model (4.9), evaluated using the first ten Fourier modes; blue line, H4; red line, H6; black line, H7. (*b*) The same data as in panel (*a*) but plotted logarithmically. The dashed line is the Wong & Parker (2006) version of the Meyer-Peter and Müller (MPM) formula for turbulent flows: $q_p/q_i = 4.93\ (\theta - \theta_c)^{1.6}$.

encodes the relaxation of the sediment bed (which will be discussed below) is superior when compared with models based on a local relationship. Let us mention that aeolian sand transport models that account for a similar phase shift between topology and shear stress (link with the sediment flux through the Exner equation) have been shown to provide better prediction of the formation and evolution of dunes (Andreotti *et al.* 2002; Kroy, Sauermann & Herrmann 2002; Hersen *et al.* 2004).

Figure 12 shows the variation of the non-dimensional sediment flow rate resolved along the ripple profile as a function of the non-dimensional local Shields number $\tilde{\theta}_b$. We note that, in plotting the data points in the figure, $\langle \tilde{q}_p \rangle_{zt}$ is averaged over bins of width $\varDelta_V$ that match those used to compute $\tilde{\tau}_b$. The above-discussed complexity of the relationship is evident, which classical models such as that by Meyer-Peter & Müller (1948) fail to predict. It is only for the blue coloured symbols (corresponding to the blue demarcated region in figure 8 roughly upstream of the maximum shear-stress location) that the particle flow rate predicted by MPM formula approximately matches the data. Note that, as has been reported in KU2017 and is reproduced in figure 12(*b*), the space- and time-averaged particle flow rate is nevertheless well predicted by the Wong & Parker (2006) version of the Meyer-Peter & Müller (1948) power-law formula. On the other hand, as demonstrated in the figure, the scale-resolved, phase-shift accounting model (4.9), evaluated using ten modes, provides a reasonable representation of the data.

For a closer inspection of the sediment-bed response to the spatial changes in the shear stress, it is essential to distinguish the particle flux within the mobile transport layer from possible contributions due to suspended particles, in particular in the re-circulation region downstream of the crest. Moreover, although minute in magnitude, the motion deep within the bulk sediment bed is not directly related to the boundary shear stress but rather to the form-induced pressure gradient from the outer flow (Mazzuoli *et al.* 2019). To this end, we have decomposed $\langle \tilde{q}^{2D}_{p,x} \rangle_{zt}$ into four transport mode regions (cf. figure 13). First we distinguish between the 'resting' sediment bed and the active mobile sediment layer – usually termed in the community as the 'transport layer' – by defining an interface where the phase-averaged solid volume fraction $\tilde{\phi}_p$ equals the mean value in the resting bed $\varPhi_{bed}$

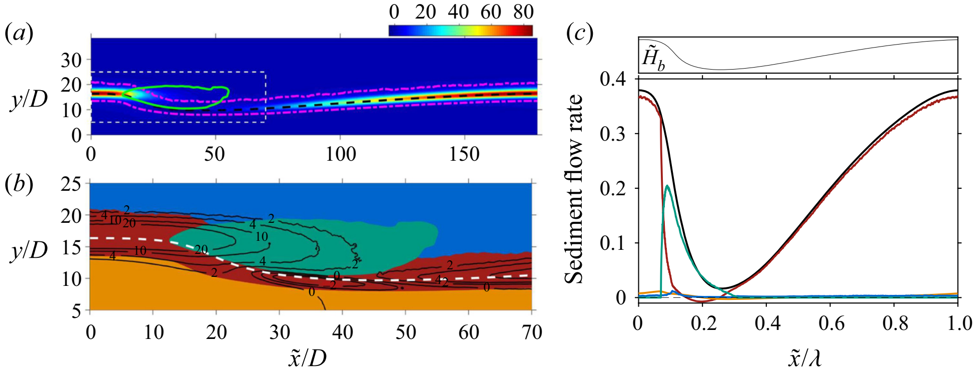

Figure 13. (*a*) Phase-averaged two-dimensional particle flow rate (streamwise component) per unit area, $\langle \tilde{q}^{2D}_{p,x} \rangle_{zt}$, normalised by $U_g D^2$ for case H7. The pink dashed-dot curves indicate the boundaries of the bedload transport layer. The green solid curve demarcates the particle inertia dominated region. The fluid–bed interface is indicated by the black dashed curve. (*b*) Contour lines of $\langle \tilde{q}^{2D}_{p,x} \rangle_{zt} / U_g D^2$ in the region downstream of the ripple crest (the box region shown in panel (*a*)). The different sediment particle transport regions are colour coded as follows: orange, quasi-stationary sediment bed; maroon, bedload transport layer; blue, dilute suspension region; green, particle inertia dominated region. (*c*) $\langle \tilde{q}_p \rangle_{zt} / q_i$ of case H7 (thick black line) decomposed into the different sediment flow rate components. Line colour coding is the same as for panel (*b*).

(the interface between the orange and red regions in figure 13*b*). More precisely, for a streamwise position $\tilde{x}$, we fit a straight line to $\tilde{\phi}_p$ in the interval between the wall-normal locations where $\tilde{\phi}_p = 0.1$ and $\tilde{\phi}_p = 0.4$. Then, we pick the wall-normal location $y_b(\tilde{x})$ where the fitted line crosses the value Φ_{bed}. The motivation for the above definition stems from the solid volume-fraction-dependent rheology of the sheared sediment layer in which $\tilde{\phi}_p$ tends to Φ_{bed} as the local shear rate tends to zero (Boyer, Guazzelli & Pouliquen 2011). We subsequently demarcate the transport layer from the dilute suspension region by the interface located at $y_t(\tilde{x})$. In the latter, sediments are transported mainly in suspended mode (the blue region in figure 13*b*). The interface is defined based on a threshold value of the phase-averaged wall-normal inter-particle collision force $\langle \tilde{f}^{C}_{p,y} \rangle_{zt}$ (Scherer *et al.* 2020). Additionally, we distinguish the sediment flux immediately downstream of the ripple crest that is dominated by fully suspended particles that have retained a substantial amount of their momentum from upstream. This 'inertial sediment flux' region is demarcated based on a threshold value of the phase-averaged streamwise hydrodynamic force acting on the particles $\langle \tilde{f}^{H}_{p,x} \rangle_{zt}$ as particles are characterised by increased negative $\langle \tilde{f}^{H}_{p,x} \rangle_{zt}$ due to fluid-drag-induced deceleration. The inertial region is shown by the green region in figure 13(*b*). Defining the inertial region by an indicator function I_r that has a value of unity in the region and zero elsewhere, the particle flow rate within the transport layer and excluding the inertial region can be defined as

$$\langle \tilde{q}^{TL}_p \rangle_{zt}(\tilde{x}) = \int_{y_b(\tilde{x})}^{y_t(\tilde{x})} \langle \tilde{q}^{2D}_{p,x} \rangle_{zt} (1 - I_r)\, \mathrm{d}y. \tag{4.10}$$

The other contributions to $\langle \tilde{q}_p \rangle_{zt}$ are analogously defined. As can be seen from figure 13(*c*), $\langle \tilde{q}_p \rangle_{zt}$ is dominated by $\langle \tilde{q}^{TL}_p \rangle_{zt}$ in almost the entire ripple profile, except in the region immediately downstream of the crest. It is also noteworthy that $\langle \tilde{q}^{TL}_p \rangle_{zt}$ attains very small but negative values in the recirculation region.

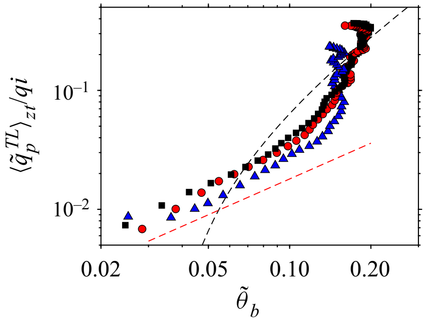

Figure 14. Particle flow rate in the bedload transport layer $\langle \tilde{q}_p^{TL} \rangle_{zt}$ as a function of the local Shields number $\tilde{\theta}$: ▲, blue, H4; ●, red, H6; ■, H7. Only data points on the stoss side of the ripple are shown. The black dashed curve is the MPM formula, while the red dashed line shows a linear scaling.

In figure 14, the relationship between the local Shields number and local $\langle \tilde{q}_p^{TL} \rangle_{zt}$ is presented. Only data points corresponding to the stoss side of the ripple (defined as the region between the trough and crest) are shown. The relaxation of $\langle \tilde{q}_p^{TL} \rangle_{zt}$ to changes in $\tilde{\theta}_b$ is evident from the figure: in the 'shear-stress recovery' region, i.e. the region where the shear stress increases sharply from its almost zero value downstream of the trough (the red interval in figure 8), $\langle \tilde{q}_p^{TL} \rangle_{zt}$ is seen to increase modestly exhibiting a linear relationship with $\tilde{\theta}_b$, which is smaller when compared with the 3/2 power law that is expected to hold in equilibrium. Subsequently, while the shear-stress evolution reaches a plateau (green and blue regions in figure 8), the particle flux sharply increases and then tends towards a 3/2 power-law relationship in the blue region.

4.4. *Relaxation of the sediment flux*

Although it is established that the phase lag between $\tilde{\tau}_b$ and $\langle \tilde{q}_p^{TL} \rangle_{zt}$ is a consequence of the inertia of the subaqueous sediment bed, there has been no direct measurement of the relaxation effect. In the following, we evaluate this quantity from our DNS data, independent of the influence of the bedforms. Let us recall that we have initiated the simulations by first developing a turbulent flow over a macroscopically flat bed composed of stationary particles. After the coupled fluid–solid simulations were switched on by allowing the particles to move, the erosion–deposition process ramps up over a relatively short time in response to the shear imposed by the flow (see detailed description of the startup procedure in Kidanemariam & Uhlmann 2014*a*). Our startup procedure allows us to investigate the sediment flux relaxation behaviour during the first instants of the sediment grain motion. To this end, we have computed the space-averaged instantaneous particle flow rate within the transport layer given as

$$\langle q_p^{TL} \rangle_{xz}(t) = \int_{y_b(t)}^{y_t(t)} \langle u_p \phi_p \rangle_{xz} \, \mathrm{d}y, \tag{4.11}$$

for the time interval before any bed patterns have formed. Here, y_b and y_t are the lower and upper extents of the transport layer and are defined in § 4.2. Note that, during this stage, the transients of all the simulation cases reported in KU2017 are statistically identical. Therefore, in order to increase the sample size, we have analysed the data corresponding to case H48 in KU2017. That case possesses a relatively large domain size ($L_x = 48H$) with over a million particles and is suitable to scrutinise the transient evolution of the particle

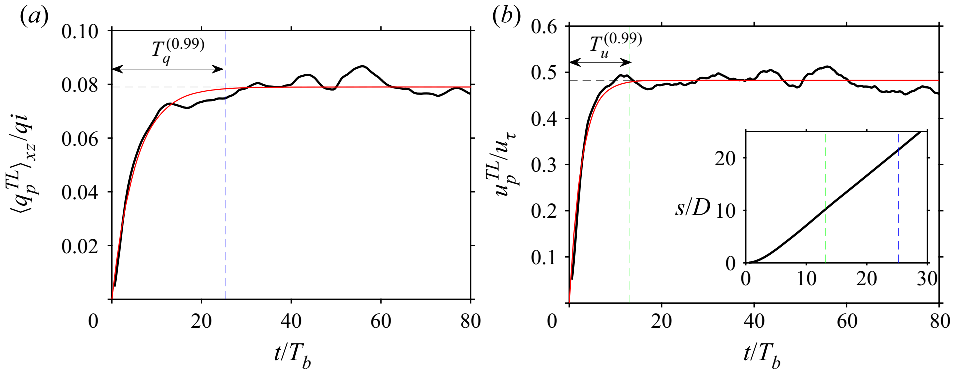

Figure 15. (a) Time evolution of the particle flow rate within the transport layer of case H48 in KU2017. The red curve is an exponential fit to the data of the form $q = q_s(1 - \exp(-t/T_q))$. ($b$) Corresponding evolution of the mean particle velocity within the transport layer along with the exponential fit $u_p = u_{p,s}(1 - \exp(-t/T_u))$. The inset shows the equivalent distance s travelled by the mobile layer as a function of time defined as $s(t) = \int_0^t u_p^{TL}\,\mathrm{d}t$. The green and blue dashed lines in the inset show $T_u^{0.99}$ and $T_q^{0.99}$ respectively, while the ordinates at which the dashed lines cross the curve $s(t)$ correspond to $L_u^{0.99}$ and $L_q^{0.99}$, respectively.

flow rate accurately. As can be seen in figure 15(a), $\langle q_p^{TL}\rangle_{xz}$ requires a finite time to attain a saturated value in this ’featureless bed’ interval (once bedforms emerge the particle flow rate increases again in accordance with the temporal increase of the bottom friction). In order to compute a characteristic time for the transient behaviour we fit an exponential of the form

$$q = q_s(1 - \exp(-t/T_q)), \tag{4.12}$$

with fit parameters q_s and T_q, to $\langle q_p\rangle_{xz}$ in the interval $0 < t/T_b < 80$. Our analysis follows that by Andreotti, Claudin & Pouliquen (2010) and Pähtz *et al.* (2015) who have carried out experiments and DEM simulations of aeolian sand transport saturation length, respectively. Subsequently, we define a transient time scale $T_q^{0.99}$ as the time required for q to reach $0.99q_s$. It turns out that, for case H48, $q_s \approx 0.08q_i$, $T_q \approx 5.4T_b$ and $T_q^{0.99} \approx 25T_b$ (cf. figure 15a). Furthermore, $T_q^{0.99}$ can be translated into an equivalent length scale $L_q^{0.99}$ as

$$L_q^{0.99} = \int_0^{T_q^{0.99}} u_p^{TL}\,\mathrm{d}t, \tag{4.13}$$

where u_p^{TL} is the average instantaneous particle velocity within the bedload transport layer, given as

$$u_p^{TL}(t) = \frac{\langle q_p^{TL}\rangle_{xz}}{\varPhi_p^{TL}}. \tag{4.14}$$

Here, $\varPhi_p^{TL}$ is the volume of particles in the transport layer per unit horizontal area, *viz.*

$$\varPhi_p^{TL}(t) = \int_{y_b(t)}^{y_t(t)} \langle \phi_p\rangle_{xz}\,\mathrm{d}y. \tag{4.15}$$

The evolution of u_p^{TL} shown in figure 15(b) exhibits a similar relaxation trend as $\langle q_p^{TL}\rangle_{xz}$ albeit at a shorter time scale. We emphasise that the relaxation of u_p^{TL} is mainly controlled by the particle acceleration/deceleration due to fluid drag and inter-particle interaction within the transport layer while that of $\langle q_p^{TL} \rangle_{xz}$ is controlled both by the relaxation of u_p^{TL} and that of the mobile particle number density, or equivalently $\varPhi_p^{TL}$ (Charru 2006; Pähtz *et al.* 2013, 2014). As shown in the inset of figure 15(*b*), $L_q^{0.99} \approx 20D$ and agrees very well with the computed average phase shift between the boundary shear stress and the particle flow rate over the bedforms, thus suggesting the link between the two. The relaxation of u_p^{TL} by itself is an important model ingredient (cf. Pähtz *et al.* 2013, 2014, 2015) and analogous to the particle flow rate, we fit the same exponential function defined with parameters $u_{p,s}$ and T_u (or equivalently $T_u^{0.99}$) to the evolution of u_p^{TL}. Incidentally, $u_{p,s} \approx 0.49 u_\tau$, $T_u \approx 2.8 T_b$ and $T_u^{0.99} \approx 13 T_b$. Furthermore, $T_u^{0.99}$ can be translated into an equivalent length scale $L_u^{0.99}$, and, as shown in the inset of figure 15(*b*), it turns out that $L_u^{0.99} \approx 10D$. To the best of our knowledge, there is no direct experimental measurement of the relaxation length/time scales of subaqueous sediment to compare our results with. The quantity is usually reconstructed from measured dune shape and migration velocity (cf. Fourrière *et al.* 2010; Franklin & Charru 2011).

5. Conclusion

We have numerically investigated the turbulent flow and sediment grain motion in an open-channel flow configuration over a thick, freely evolving, subaqueous sediment bed featuring two-dimensional transverse ripples. The fluid–solid interaction has been faithfully accounted for via particle-resolved direct numerical simulation, while the sediment bed has been represented by a large number of mobile finite-size spherical particles. The simulation data analysed in the present study are identical to those in our recent work (Kidanemariam & Uhlmann 2017). The latter study was exclusively devoted to the description of the initiation and evolution aspects of the sediment patterns. In the present contribution, we have extended our analysis, focusing on the unsteady and non-homogeneous fluid flow over the bedforms, the main driving force in their formation. Our analysis has also equally focused on the associated sediment grain motion, the process by which a sheared sediment bed gives way to the formation and evolution of the bedforms.

At the chosen moderate Reynolds number and super-critical Shields number values, the flow erodes and mobilises an initially featureless sediment bed leading to the formation of ripples that are, on average, perpendicular to the mean flow direction and that migrate downstream. The bed evolution in turn strongly modifies the flow from its initial statistically one-dimensional state towards a two-dimensional state. The conditions of our simulations have allowed us to constrain the temporal growth of the ripples (by limiting the computational box length), forcing the patterns to maintain their shape and size, and migrate at a statistically constant velocity. This in turn has allowed us to run simulations of the steady ripple migration regime over a sufficiently long temporal duration. Subsequently, we have performed ripple-conditioned phase averaging of the generated fluid and particle data and analysed the spatio-temporal correlation of the turbulent flow with the sediment bed.

The basic features of the two-dimensional phase-averaged mean flow were found to be, in general, in good resemblance to the flow over fixed dunes for which there exists extensive literature (Best 2005). However, to the best of our knowledge, there is no detailed measurement of the corresponding mean particle velocity statistics within and above the sediment bed. It was evidenced that the permeable bed interface, which lies within the bedload transport layer, is subject to active mass/momentum exchange of both phases as a result of erosion and deposition of sediment particles and the fluid motion therein.

The phase-averaged mean particle velocity is smaller than that of the fluid over most of the ripple surface, except in the re-circulation region where it exhibits the opposite behaviour. It should be noted that the apparent velocity difference is mainly attributed to the preferential sampling of the buffer layer low-speed streaks by inertial particles (Kidanemariam *et al.* 2013), thus caution is advised when using such quantity in models that rely on particle drag correlations. Moreover, downstream of the crest, sediment particles carry their momentum from upstream into the re-circulation region and, due to their inertia, do not immediately adapt to the enhanced fluid drag therein, resulting in a higher mean particle velocity, and thus higher particle flow rate. In general, the observation highlights the complex particle relaxation effects in response to the spatial changes of the fluid flow.

We have further performed an evaluation of the momentum budget over moving local control volumes adapted to the shape of the ripples, in order to compute the basal shear-stress variation (at the bed interface). The accurate determination of this quantity, which is one of the main ingredients in models of sediment-bed morphology, has been an outstanding issue. Our analysis has shown that the shear stress is maximum at a location upstream of the crests exhibiting a positive phase shift with respect to the ripple geometry. Likewise, the location of the minimum shear stress is upstream of the ripple trough. For the considered ripple sizes (mean wavelength λ in the range $100D$–$180D$), the average phase shift lies in the range $16D$–$19D$. The phase advance of the shear stress, which is a consequence of fluid inertia, is known to be responsible for the instability of an erodible sediment bed (Charru *et al.* 2013).

As a consequence of the sediment mass conservation, the volumetric particle flow rate, integrated over the whole channel depth but resolved in the streamwise direction, evolves essentially in phase with the ripple geometry, thus lags the shear stress by practically the same phase-shift amount as that of the topology, measuring $18D$ to $19D$. This observation is evidence that expressing the spatial structure of the particle flux as a function of the local shear stress by an algebraic expression is not adequate. Indeed, classical empirical power laws such as that by Wong & Parker (2006), which have been shown to be robust in predicting the space- and time-averaged particle flow rate over the same ripples (Kidanemariam & Uhlmann 2017), fail to capture the observed spatial variability. Nevertheless, a scale-resolved, simplified relationship between the bottom shear stress and the particle flow rate that incorporates a phase-shift parameter, is shown to reasonably represent the DNS data. This has been shown by comparing the amplitude and phase shift of the dominant Fourier modes of the boundary shear stress and those of the particle flow rate. It is found that corresponding amplitudes of the two quantities exhibit a power-law relationship with exponent $3/2$, while the relative phase shift (in radians) remains essentially independent of the wavenumber.

It has been long recognised that the phase lag of the particle flux with respect to the shear stress is a consequence of sediment inertia. That is, an erodible sediment bed needs some time/distance to adapt to change in flow conditions. This sediment relaxation behaviour is usually expressed in terms of a saturation length scale (Sauermann *et al.* 2001; Charru 2006). The saturation length is believed to be an important controlling parameter of the initial ripple size and has been included in a number of models (cf. the introduction § 1 and references therein). Nevertheless, there has been no direct measurement of this quantity, in particular for subaqueous sediment transport (Duran Vinent *et al.* 2019). This in turn has impeded a fuller understanding of the relevant processes and mechanisms. Our numerical data set has, for the first time, allowed us to evaluate this quantity accurately. To this end, we have investigated the link of the observed phase lag of the particle flow rate with respect to the boundary shear stress over the bedforms to that of the sediment-bed relaxation behaviour. By monitoring the evolution of the particle flow rate within the transport layer in the first few bulk time units of the simulation interval (before any bedforms have emerged), it was found that, for the parameter values considered, the sheared transport layer gets mobilised from the initial state of zero particle flow rate towards some steady-state value within a time lag of approximately 25 bulk time units. By evaluating the temporal evolution of particle velocity, the saturation length, which measures approximately $20D$, is found to be in close agreement with the phase lag measured over the fully developed ripples.

The saturation length of the particle flux, computed for the current parameter point to be approximately $20D$, is clearly larger than that of the particle velocity, which measures approximately $10D$. That is, the particle flux needs longer time to saturate than the particle velocity (similar results were also obtained from DEM simulations of aeolian sediment transport by Pähtz *et al.* 2015). Note that the relaxation of the sediment flux is a consequence of multiple inter-linked mechanisms that include the relaxation of the number density of the mobile sediment grains within the transport layer (or equivalently the mass of the mobilised sediment particles per unit area) and the relaxation of the sediment grain motion. The saturation of the mobile sediment number density is conjectured to be governed by the net rate of particle entrainment and deposition between the transport layer and the stationary sediment bed beneath. The saturation is said to scale with the deposition length, proportional to $(u_\tau/u_s)D$, u_s being the particle settling velocity (Charru 2006; Charru & Hinch 2006). On the other hand, the temporal evolution of the particle velocity is modulated by the inertial response of the mobilised particles to the hydrodynamic forces and inter-particle collisions (Fourrière *et al.* 2010; Andreotti *et al.* 2011). The latter authors consider the effect of hydrodynamic drag only and they propose a dominant drag length (i.e. the length needed for a particle to reach its saturation value) proportional to $(\rho_p/\rho_f)D$. The fact that the present study considers only one parameter point makes it difficult to assess the scaling of the sediment flux relaxation with respect to the above length scales. Interestingly, our computed value of the relaxation length (in particular for the saturation of the particle velocity) is comparable to the saturation length L_{sat} estimated by Fourrière *et al.* (2010). The latter authors estimate L_{sat} (indirectly from experimental measurements of initial ripple wavelengths) in the range between 7 and 15 grain diameters, agreeing very well with our computed value of $L_u^{(0.99)}$ but slightly underestimating $L_q^{(0.99)}$, consistent with their model assumption.

Finally, we note that a single parameter point (in terms of flow Reynolds number, particle size, density ratio and Shields number) is considered in the present study. Although desirable, it was not possible to sweep the parameter space and thereby study the regime dependence of the observed flow and particle motion behaviour due to the immense computational cost. In particular, an assessment of model assumptions that link the observed bottom shear-stress variation with the sediment-bed dynamics is only possible when the simulated parameter space is extended. This will allow us, for instance, to investigate the influence of the Reynolds number or the channel confinement on the shear-stress parameters $\mathcal{A}_j$ and $\mathcal{B}_j$ (4.6). Furthermore, additional simulations are required to study the mechanisms behind the sediment-bed relaxation behaviour (both at the grain scale and collectively) and its dependence on the Reynolds number and particle quantities such as the density ratio and Galileo number. This will allow us to evaluate the relative importance of the deposition length and the drag length on the saturation length and evaluate sophisticated models such as that by Pähtz *et al.* (2013) more rigorously in the subaqueous setting. Finally, although the flow over stationary imposed dunes has striking similarity to the flow over evolving bedforms, the former configuration falls short of representing the 'four-way' coupled interaction between the flow and the dynamic sediment bed. An assessment of the validity of such a simplified configuration in representing the flow over evolving dunes needs to be done. These tasks remain to be addressed in future work.

Acknowledgements. Part of the simulations have been carried out on SuperMUC at the Leibniz Supercomputing Center (LRZ) of the Bavarian Academy of Science and Humanities. The simulations were also partly performed on the computational resource ForHLR I/II of the Steinbuch Centre for Computing (SCC) funded by the Ministry of Science, Research and the Arts Baden-Württemberg and DFG. The computer resources, technical expertise and assistance provided by the staff at these computer centres are thankfully acknowledged.

Funding. This work was supported by the German Research Foundation (DFG) through grant UH242/2-1.

Declaration of interests. The authors report no conflict of interest.

Author ORCIDs.
Aman G. Kidanemariam https://orcid.org/0000-0003-4276-671X;
Markus Scherer https://orcid.org/0000-0002-6301-4704;
Markus Uhlmann https://orcid.org/0000-0001-7960-092X.

Appendix A. Definition of averaging operators

A.1. *Plane and time averaging*

Let us first define an indicator function $\phi_f(\boldsymbol{x}, t)$ for the fluid phase that has a value of unity if $\boldsymbol{x}$ lies inside $\varOmega_f(t)$ – the part of the computational domain $\varOmega$ that is occupied by the fluid at time t – or zero otherwise

$$\phi_f(\boldsymbol{x}, t) = \begin{cases} 1 & \text{if} \quad \boldsymbol{x} \in \varOmega_f(t) \\ 0 & \text{else} \end{cases} . \tag{A1}$$

Similarly, an individual particle indicator function $\phi_p^{(l)}$ is defined as

$$\phi_p^{(l)}(\boldsymbol{x}, t) = \begin{cases} 1 & \text{if} \quad \boldsymbol{x} \in \varOmega_p^{(l)}(t) \\ 0 & \text{else} \end{cases} , \tag{A2}$$

where $\varOmega_p^{(l)}(t)$ is the volume occupied by the lth particle at time t. Thus, an instantaneous discrete counter of fluid sample points in a wall-parallel plane at a given wall distance y_j and time t^m is defined as

$$n_{xz}(y_j, t^m) = \sum_{i=1}^{N_x} \sum_{k=1}^{N_z} \phi_f(\boldsymbol{x}_{ijk}, t^m), \tag{A3}$$

where N_x and N_z are the number of grid nodes in the streamwise and spanwise directions, respectively, and $\boldsymbol{x}_{ijk} = (x_i, y_j, z_k)^{\mathrm{T}}$ denotes a discrete grid position. Furthermore, a discrete counter of fluid sample points in a wall-parallel plane at a given wall distance y_j, sampled over N_t number of time records, is defined as

$$n(y_j) = \sum_{m=1}^{N_t} n_{xz}(y_j, t^m). \tag{A4}$$

Consequently, the ensemble averages of an Eulerian quantity $\boldsymbol{\xi}_f$ of the fluid phase over wall-parallel planes, while considering only grid points located in the fluid domain, are defined as

$$\langle \boldsymbol{\xi}_f \rangle_{xz}(y_j, t^m) = \frac{1}{n_{xz}(y_j, t^m)} \sum_{i=1}^{N_x} \sum_{k=1}^{N_z} \phi_f(\boldsymbol{x}_{ijk}, t^m)\, \boldsymbol{\xi}_f(\boldsymbol{x}_{ijk}, t^m) \tag{A5}$$

and

$$\langle \boldsymbol{\xi}_f \rangle_{xzt}(y_j) = \frac{1}{n(y_j)} \sum_{m=1}^{N_t} n_{xz}(y_j, t^m) \langle \boldsymbol{\xi}_f \rangle_{xz}(y_j, t^m), \tag{A6}$$

where the operator $\langle \cdot \rangle_{xz}$ in (A5) indicates an instantaneous plane average and the operator $\langle \cdot \rangle_{xzt}$ in (A6) indicates an average over plane and time. The corresponding averaging operators for a particle related Eulerian quantity $\boldsymbol{\xi}_p$ are analogously defined as

$$\langle \boldsymbol{\xi}_p \rangle_{xz}(y_j, t^m) = \frac{1}{N_x N_z - n_{xz}(y_j, t^m)} \sum_{i=1}^{N_x} \sum_{k=1}^{N_z} \left(1 - \phi_f(\boldsymbol{x}_{ijk}, t^m)\right) \boldsymbol{\xi}_p(\boldsymbol{x}_{ijk}, t^m), \tag{A7}$$

and

$$\langle \boldsymbol{\xi}_f \rangle_{xzt}(y_j) = \frac{1}{N_x N_z N_t - n(y_j)} \sum_{m=1}^{N_t} \left(N_x N_z - n_{xz}(y_j, t^m)\right) \langle \boldsymbol{\xi}_p \rangle_{xz}(y_j, t^m). \tag{A8}$$

A.2. *Averaging in the spanwise direction and time*

For the purpose of the phase averaging introduced in Appendix B, we introduce averaging operators only in the spanwise direction and in time. First, a two-dimensional discrete counter of fluid sample points in the x–y plane at points x_i and y_j is defined as

$$n_{zt}(x_i, y_j) = \sum_{k=1}^{N_z} \sum_{m=1}^{N_t} \phi_f(\boldsymbol{x}_{ijk}, t^m). \tag{A9}$$

Consequently, the ensemble average of an Eulerian quantity $\boldsymbol{\xi}_f$ of the fluid phase over spanwise-perpendicular planes, while considering only grid points located in the fluid domain, is defined as

$$\langle \boldsymbol{\xi}_f \rangle_{zt}(x_i, y_j) = \frac{1}{n_{zt}(x_i, y_j)} \sum_{k=1}^{N_z} \sum_{m=1}^{N_t} \phi_f(\boldsymbol{x}_{ijk}, t^m)\, \boldsymbol{\xi}_f(\boldsymbol{x}_{ijk}, t^m). \tag{A10}$$

Similarly, the particle related Eulerian field defined in (B5) is averaged in the spanwise direction and time as follows:

$$\langle \boldsymbol{\xi}_p \rangle_{zt}(x_i, y_j) = \frac{1}{N_z N_t - n_{zt}(x_i, y_j)} \sum_{m=1}^{N_t} \sum_{k=1}^{N_z} \sum_{l=1}^{N_p} \phi_p^{(l)}(\boldsymbol{x}_{ijk}, t^m) \boldsymbol{\xi}_p^{(l)}(t^m), \tag{A11}$$

where N_p is the total number of particles.

Appendix B. Phase averaging

In this section, we specify the ripple-conditioned phase-averaging procedure. The phase-averaged fluid–bed interface is defined as follows:

$$\tilde{H}_b(\tilde{x}) = \langle h_b(\tilde{x}, t)\rangle_t, \tag{B1}$$

where $\tilde{x}$ is the x-coordinate in a frame of reference that is moving at the average migration velocity

$$\tilde{x} = x - u_D(t - t_s), \tag{B2}$$

where u_D is the average migration velocity of the patterns and t_s is the starting time of the steady ripple propagation interval; u_D is determined from the shift of the maximum of the space–time correlation function between the fluid–bed interface fluctuation at times t_s and t (see KU2017 for the precise definition of u_D). Similarly, we define the phase-shifted fluid and particle velocity fields as

$$\tilde{\boldsymbol{u}}_f = \boldsymbol{u}_f(\tilde{x}, y, z, t), \tag{B3}$$

$$\tilde{\boldsymbol{u}}_p = \boldsymbol{u}_p(\tilde{x}, y, z, t), \tag{B4}$$

where $\boldsymbol{u}_p$ is a surrogate instantaneous Eulerian particle field that contains information regarding the Lagrangian velocity of all particles at time t, *viz.*

$$\boldsymbol{u}_p(x, y, z, t) = \sum_{l=1}^{N_p} \phi_p^{(l)}(x, y, z, t)\boldsymbol{u}_p^{(l)}(t). \tag{B5}$$

Here, $\phi_p^{(l)}$ is a particle indicator function that has a value of unity if the position $\boldsymbol{x}$ lies inside the domain occupied by the lth particle at time t and is zero otherwise (cf. Appendix A for the precise definition). Other phase-shifted fluid and particle quantities are similarly defined. Subsequently, ripple-conditioned statistics, which are function of both $\tilde{x}$ and y, are computed by applying standard averaging of the phase-shifted fluid and particle quantities, in the spanwise direction z and over time (over the number of available fluid and particle snapshots). For instance, the phase-averaged fluid and particle velocities are defined, respectively, as

$$\tilde{\boldsymbol{U}}_f(\tilde{x}, y) = \langle \tilde{\boldsymbol{u}}_f\rangle_{zt}, \tag{B6}$$

$$\tilde{\boldsymbol{U}}_p(\tilde{x}, y) = \langle \tilde{\boldsymbol{u}}_p\rangle_{zt}. \tag{B7}$$

The instantaneous phase-shifted fluid and particle velocities are decomposed in the usual way into mean and fluctuating components

$$\tilde{\boldsymbol{u}}_f(\tilde{x}, y, z, t) = \tilde{\boldsymbol{U}}_f(\tilde{x}, y) + \tilde{\boldsymbol{u}}_f{}'(\tilde{x}, y, z, t) \tag{B8}$$

$$\tilde{\boldsymbol{u}}_p(\tilde{x}, y, z, t) = \tilde{\boldsymbol{U}}_p(\tilde{x}, y) + \tilde{\boldsymbol{u}}_p'(\tilde{x}, y, z, t), \tag{B9}$$

respectively. Using the notation $\boldsymbol{ab}$ with components a_ib_j as the dyadic product of two vectors $\boldsymbol{a}$ and $\boldsymbol{b}$, covariances of the fluid and particle velocity fluctuation tensors are defined similarly as $\langle \tilde{\boldsymbol{u}}_f{}'\tilde{\boldsymbol{u}}_f{}'\rangle_{zt}$ and $\langle \tilde{\boldsymbol{u}}_p'\tilde{\boldsymbol{u}}_p'\rangle_{zt}$, respectively. The averaging operator $\langle\cdot\rangle_{zt}$, which applies differently to the fluid and particle fields by taking into account the fraction of space occupied by the respective phases, is precisely defined in Appendix A.

Let us note that, due to the streamwise periodicity, further averaging in the streamwise direction results in the mean velocities of the respective phases that would be obtained

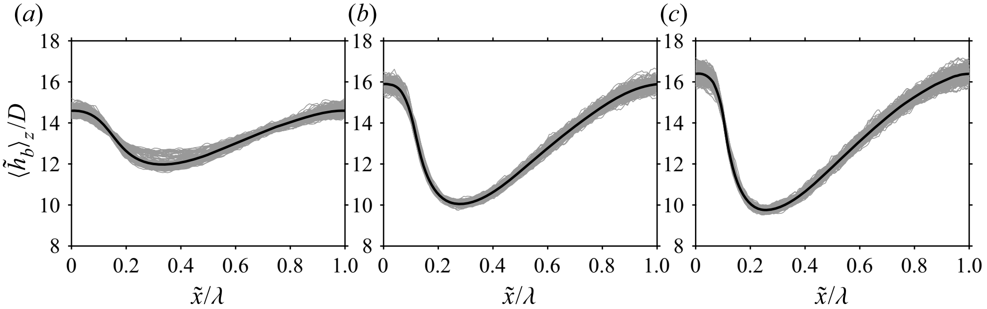

Figure 16. Sediment-bed-height profiles $\langle \tilde{h}_b \rangle_z$ at various instants over the steady-state interval (grey curves). The corresponding phase-averaged fluid–bed interface $\langle \tilde{h}_b \rangle_{zt}$ is indicated as a black curve: (*a*) H4; (*b*) H6; (*c*) H7.

from standard averaging over wall-parallel planes and time (taking into account the solid/fluid volume fraction). For instance, $\langle \tilde{\boldsymbol{U}}_f(\tilde{x}, y) \rangle_x = \boldsymbol{U}_f(y)$, where $\boldsymbol{U}_f \equiv \langle \boldsymbol{u}_f \rangle_{xzt}$ is the plane- and time-averaged mean flow field. However, this is not true for the velocity fluctuation covariances. That is,

$$\langle \boldsymbol{u}'_f \boldsymbol{u}'_f \rangle_{xzt}(y) = \langle \langle \tilde{\boldsymbol{u}}_f{}' \tilde{\boldsymbol{u}}_f{}' \rangle_{zt} \rangle_x(y) + \langle \langle \tilde{\boldsymbol{u}}_f{}'' \tilde{\boldsymbol{u}}_f{}'' \rangle_{zt} \rangle_x(y), \tag{B10}$$

where the first term on the right-hand side of (B10) represents the turbulent Reynolds stresses while the second term corresponds to the form-induced (dispersive) contribution that results from the deflection of the mean streamlines from the streamwise direction (Nikora *et al.* 2007*a*). The dispersive stress is recovered from the ripple-conditioned statistics as

$$\langle \tilde{\boldsymbol{u}}_f{}'' \tilde{\boldsymbol{u}}_f{}'' \rangle_{zt}(\tilde{x}, y) = \tilde{\boldsymbol{U}}_f \tilde{\boldsymbol{U}}_f(\tilde{x}, y) - \boldsymbol{U}_f \boldsymbol{U}_f(y). \tag{B11}$$

Finally, let us define the phase-averaged two-dimensional solid volume fraction

$$\tilde{\phi}_p(\tilde{x}, y) = \left\langle \sum_{l=1}^{N_p} \phi_p^{(l)}(\tilde{x}, y, z, t) \right\rangle_{zt}. \tag{B12}$$

Figure 16 illustrates the phase-averaging procedure by showing the spatial evolution of the sediment-bed height for different time instants over the considered steady-state interval of the three cases. It can be seen that all the profiles collapse to within a scatter of approximately one particle diameter. The phase-averaged sediment-bed height $\tilde{H}_b$ is also shown for reference.

Both fluid and particle statistics have been computed considering the same steady-evolution interval (cf. table 2). However, the frequency at which statistics are accumulated is different. During our simulations, we typically record particle-related quantities at intervals of a few computational time steps, while full instantaneous flow field snapshots are recorded at much coarser time intervals (due to the immense storage requirement). Then dune-conditioned statistics are computed over the available particle and flow field snapshots.

Appendix C. Plane-averaged streamwise momentum balance

Here, we evaluate the plane- and time-averaged streamwise momentum equation to confirm the linearity of the total shear-stress profile across the entire channel depth.

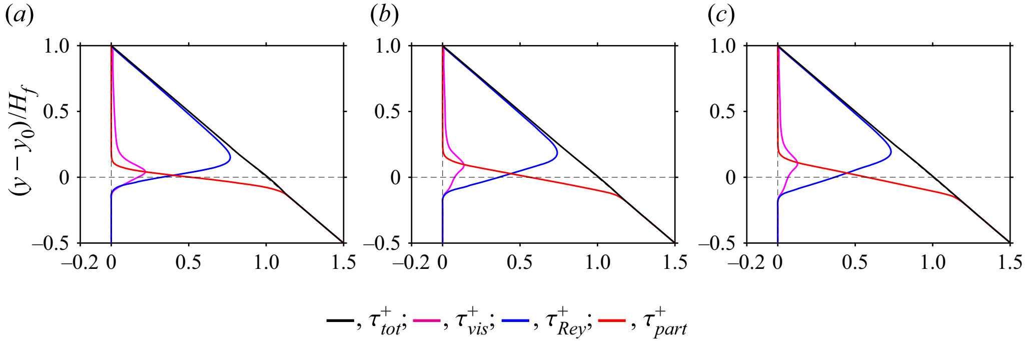

Figure 17. Wall-normal profiles of the different contributions to the total shear stress computed based on the run-time accumulated plane-averaged statistics: (*a*) H4; (*b*) H6; (*c*) H7.

Since the driving pressure gradient is balanced by the sum of the fluid shear stress and stress contribution from the fluid–particle interaction, the streamwise momentum balance (when integrated over the entire domain comprising the fluid and particles) reduces to

$$-\langle \varPi \rangle_t (L_y - y) = \rho_f \nu \partial_y \langle u \rangle_{xzt} - \rho_f \langle u'v' \rangle_{xzt} + \int_y^{L_y} \langle f_x \rangle_{xzt} \, \mathrm{d}y. \tag{C1}$$

Here, $\langle u \rangle_{xzt}$ is the mean composite velocity, and $\langle u'v' \rangle_{xzt}$ is the covariance with respect to $\langle u \rangle_{xzt}$. Note that $\langle u'v' \rangle$ represents both the turbulent and form-induced fluctuations. The last term on the right-hand side of (C1) represents the fluid–solid interaction. Figure 17 shows wall-normal profiles of the different contributions to the total shear stress for the three simulated cases. The match with the linear profile indicates that the flow is in a statistically steady state in the considered steady ripple evolution interval.

REFERENCES

ANDREOTTI, B. & CLAUDIN, P. 2013 Aeolian and subaqueous bedforms in shear flows. *Phil. Trans. A. Math. Phys. Engng Sci.* **371** (2004), 20120364.

ANDREOTTI, B., CLAUDIN, P., DEVAUCHELLE, O., DURÁN, O. & FOURRIÈRE, A. 2011 Bedforms in a turbulent stream: ripples, chevrons and antidunes. *J. Fluid Mech.* **690**, 94–128.

ANDREOTTI, B., CLAUDIN, P. & DOUADY, S. 2002 Selection of dune shapes and velocities. Part 1: dynamics of sand, wind and barchans. *Eur. Phys. J.* B **28** (3), 321–339.

ANDREOTTI, B., CLAUDIN, P. & POULIQUEN, O. 2010 Measurements of the aeolian sand transport saturation length. *Geomorphology* **123** (3–4), 343–348.

BELCHER, S.E. & HUNT, J.C.R. 1998 Turbulent flow over hills and waves. *Annu. Rev. Fluid Mech.* **30** (1), 507–538.

BENJAMIN, T.B. 1959 Shearing flow over a wavy boundary. *J. Fluid Mech.* **6** (2), 161–205.

BENNETT, S.J. & BEST, J.L. 1995 Mean flow and turbulence structure over fixed, two-dimensional dunes: implications for sediment transport and bedform stability. *Sedimentology* **42**, 491–513.

BEST, J. 2005 The fluid dynamics of river dunes: a review and some future research directions. *J. Geophys. Res.* **110** (F4), F04S02.

BOYER, F., GUAZZELLI, É. & POULIQUEN, O. 2011 Unifying suspension and granular rheology. *Phys. Rev. Lett.* **107** (18), 188301.

CHARRU, F. 2006 Selection of the ripple length on a granular bed sheared by a liquid flow. *Phys. Fluids* **18** (12), 121508.

CHARRU, F., ANDREOTTI, B. & CLAUDIN, P. 2013 Sand ripples and dunes. *Annu. Rev. Fluid Mech.* **45** (1), 469–493.

CHARRU, F. & FRANKLIN, E.M. 2012 Subaqueous barchan dunes in turbulent shear flow. Part 2. Fluid flow. *J. Fluid Mech.* **694**, 131–154.

CHARRU, F. & HINCH, E.J. 2006 Ripple formation on a particle bed sheared by a viscous liquid. Part 1. Steady flow. *J. Fluid Mech.* **550** (1), 111–121.

CHARRU, F. & LUCHINI, P. 2019 Inviscid flow separation at the crest of an erodible dune. *Phys. Rev. Fluids* **4** (3), 034304.

CHOU, Y. & FRINGER, O.B. 2010 A model for the simulation of coupled flow-bed form evolution in turbulent flows. *J. Geophys. Res.* **115** (C10), C10041.

CLAUDIN, P., CHARRU, F. & ANDREOTTI, B. 2011 Transport relaxation time and length scales in turbulent suspensions. *J. Fluid Mech.* **671**, 491–506.

CLAUDIN, P., WIGGS, G.F.S. & ANDREOTTI, B. 2013 Field evidence for the upwind velocity shift at the crest of low dunes. *Boundary-Layer Meteorol.* **148** (1), 195–206.

COLOMBINI, M. & STOCCHINO, A. 2011 Ripple and dune formation in rivers. *J. Fluid Mech.* **673**, 121–131.

DURÁN, O., ANDREOTTI, B. & CLAUDIN, P. 2012 Numerical simulation of turbulent sediment transport, from bed load to saltation. *Phys. Fluids* **24**, 103306.

DURAN VINENT, O., ANDREOTTI, B., CLAUDIN, P. & WINTER, C. 2019 A unified model of ripples and dunes in water and planetary environments. *Nat. Geosci.* **12** (5), 345–350.

ENGELUND, F. & FREDSOE, J. 1982 Sediment ripples and dunes. *Annu. Rev. Fluid Mech.* **14** (1), 13–37.

FINN, J.R., LI, M. & APTE, S.V. 2016 Particle based modelling and simulation of natural sand dynamics in the wave bottom boundary layer. *J. Fluid Mech.* **796**, 340–385.

FOURRIÈRE, A., CLAUDIN, P. & ANDREOTTI, B. 2010 Bedforms in a turbulent stream: formation of ripples by primary linear instability and of dunes by nonlinear pattern coarsening. *J. Fluid Mech.* **649**, 287–328.

FRANK-GILCHRIST, D.P., PENKO, A. & CALANTONI, J. 2018 Investigation of sand ripple dynamics with combined particle image and tracking velocimetry. *J. Atmos. Ocean. Technol.* **35** (10), 2019–2036.

FRANKLIN, E.M. & CHARRU, F. 2011 Subaqueous barchan dunes in turbulent shear flow. Part 1. Dune motion. *J. Fluid Mech.* **675** (1988), 199–222.

GADAL, C., NARTEAU, C., EWING, R.C., GUNN, A., JEROLMACK, D., ANDREOTTI, B. & CLAUDIN, P. 2020 Spatial and temporal development of incipient dunes. *Geophys. Res. Lett.* **47**, e2020GL088919.

GUAN, L., SALINAS, J.S., ZGHEIB, N. & BALACHANDAR, S. 2021 The role of bed-penetrating Kelvin–Helmholtz vortices on local and instantaneous bedload sediment transport. *J. Fluid Mech.* **911**, A50.

HERSEN, P., ANDERSEN, K., ELBELRHITI, H., ANDREOTTI, B., CLAUDIN, P. & DOUADY, S. 2004 Corridors of barchan dunes: stability and size selection. *Phys. Rev.* E **69** (1), 011304.

JACKSON, P.S. & HUNT, J.C.R. 1975 Turbulent wind flow over a low hill. *Q. J. R. Meteorol. Soc.* **101**, 929–955.

JAIN, R., TSCHISGALE, S. & FRÖHLICH, J. 2021 Impact of shape: DNS of sediment transport with non-spherical particles. *J. Fluid Mech.* **916**, A38.

JIMÉNEZ, J. 2004 Turbulent flows over rough walls. *Annu. Rev. Fluid Mech.* **36** (1), 173–196.

KENNEDY, J.F. 1963 The mechanics of dunes and antidunes in erodible-bed channels. *J. Fluid Mech.* **16** (4), 521–544.

KHOSRONEJAD, A. & SOTIROPOULOS, F. 2014 Numerical simulation of sand waves in a turbulent open channel flow. *J. Fluid Mech.* **753**, 150–216.

KIDANEMARIAM, A.G. 2015 The formation of patterns in subaqueous sediment. PhD thesis, Karlsruhe Institute of Technology.

KIDANEMARIAM, A.G., CHAN-BRAUN, C., DOYCHEV, T. & UHLMANN, M. 2013 Direct numerical simulation of horizontal open channel flow with finite-size, heavy particles at low solid volume fraction. *New J. Phys.* **15** (2), 025031.

KIDANEMARIAM, A.G. & UHLMANN, M. 2014*a* Direct numerical simulation of pattern formation in subaqueous sediment. *J. Fluid Mech.* **750**, R2.

KIDANEMARIAM, A.G. & UHLMANN, M. 2014*b* Interface-resolved direct numerical simulation of the erosion of a sediment bed sheared by laminar channel flow. *Intl J. Multiphase Flow* **67**, 174–188.

KIDANEMARIAM, A.G. & UHLMANN, M. 2017 Formation of sediment patterns in channel flow: minimal unstable systems and their temporal evolution. *J. Fluid Mech.* **818**, 716–743.

KROY, K., SAUERMANN, G. & HERRMANN, H.J. 2002 Minimal model for sand dunes. *Phys. Rev. Lett.* **88** (5), 054301.

LAJEUNESSE, E., MALVERTI, L. & CHARRU, F. 2010 Bed load transport in turbulent flow at the grain scale: experiments and modeling. *J. Geophys. Res.* **115** (F4), F04001.

LANGLOIS, V. & VALANCE, A. 2007 Initiation and evolution of current ripples on a flat sand bed under turbulent water flow. *Eur. Phys. J.* E **22** (3), 201–208.

LEARY, K.C.P. & SCHMEECKLE, M.W. 2017 The importance of splat events to the spatiotemporal structure of near-bed fluid velocity and bed load motion over bed forms: laboratory experiments downstream of a backward facing step. *J. Geophys. Res.: Earth* **122** (12), 2411–2430.

LÜ, P., NARTEAU, C., DONG, Z., CLAUDIN, P., RODRIGUEZ, S., AN, Z., FERNANDEZ-CASCALES, L., GADAL, C. & COURRECH DU PONT, S. 2021 Direct validation of dune instability theory. *Proc. Natl Acad. Sci. USA* **118** (17), e2024105118.

MADDUX, T.B., MCLEAN, S.R. & NELSON, J.M. 2003 Turbulent flow over three-dimensional dunes: 2. Fluid and bed stresses. *J. Geophys. Res.* **108**, 6010.

MAURIN, R., CHAUCHAT, J., CHAREYRE, B. & FREY, P. 2015 A minimal coupled fluid-discrete element model for bedload transport. *Phys. Fluids* **27** (11), 113302.

MAZZUOLI, M., BLONDEAUX, P., VITTORI, G., UHLMANN, M., SIMEONOV, J. & CALANTONI, J. 2020 Interface-resolved direct numerical simulations of sediment transport in a turbulent oscillatory boundary layer. *J. Fluid Mech.* **885**, A28.

MAZZUOLI, M., KIDANEMARIAM, A.G. & UHLMANN, M. 2019 Direct numerical simulations of ripples in an oscillatory flow. *J. Fluid Mech.* **863**, 572–600.

MCLEAN, S.R. & SMITH, J.D. 1986 A model for flow over two-dimensional bed forms. *ASCE J. Hydraul. Engng* **112** (4), 300–317.

MCLEAN, S.R., NELSON, J.M. & WOLFE, S.R. 1994 Turbulence structure over two-dimensional bed forms: implications for sediment transport. *J. Geophys. Res.* **99**, 12729–12747.

MEYER-PETER, E. & MÜLLER, R. 1948 Formulas for bed-load transport. In *Proceedings 2nd Meeting, Stockholm, Sweden*, pp. 39–64. IAHR.

NELSON, J.M., MCLEAN, S.R. & WOLFE, S.R. 1993 Mean flow and turbulence fields over two-dimensional bed forms. *Water Resour. Res.* **29** (12), 3935–3953.

NIKORA, V., MCEWAN, I., MCLEAN, S., COLEMAN, S., POKRAJAC, D. & WALTERS, R. 2007*a* Double-averaging concept for rough-bed open-channel and overland flows: theoretical background. *ASCE J. Hydraul. Engng* **133** (8), 873–883.

NIKORA, V., MCLEAN, S., COLEMAN, S., POKRAJAC, D., MCEWAN, I., CAMPBELL, L., ABERLE, J., CLUNIE, D. & KOLL, K. 2007*b* Double-averaging concept for rough-bed open-channel and overland flows: applications. *ASCE J. Hydraul. Engng* **133**, 884–895.

OMIDYEGANEH, M. & PIOMELLI, U. 2011 Large-eddy simulation of two-dimensional dunes in a steady, unidirectional flow. *J. Turbul.* **12**, N42.

OURIEMI, M., AUSSILLOUS, P. & GUAZZELLI, É. 2009 Sediment dynamics. Part 2. Dune formation in pipe flow. *J. Fluid Mech.* **636**, 295–319.

PÄHTZ, T., KOK, J.F., PARTELI, E.J.R. & HERRMANN, H.J. 2013 Flux saturation length of sediment transport. *Phys. Rev. Lett.* **111** (21), 218002.

PÄHTZ, T., OMERADŽIĆ, A., CARNEIRO, M.V., ARAÚJO, N.A.M. & HERRMANN, H.J. 2015 Discrete element method simulations of the saturation of aeolian sand transport. *Geophys. Res. Lett.* **42** (6), 2063–2070.

PÄHTZ, T., PARTELI, E.J.R., KOK, J.F. & HERRMANN, H.J. 2014 Analytical model for flux saturation in sediment transport. *Phys. Rev.* E **89** (5), 052213.

RAUPACH, M.R. & SHAW, R.H. 1982 Averaging procedures for flow within vegetation canopies. *Boundary-Layer Meteorol.* **22** (1), 79–90.

RICHARDS, K.J. 1980 The formation of ripples and dunes on an erodible bed. *J. Fluid Mech.* **99** (3), 597–618.

RODRIGUEZ-ABUDO, S. & FOSTER, D.L. 2014 Unsteady stress partitioning and momentum transfer in the wave bottom boundary layer over movable rippled beds. *J. Geophys. Res.: Oceans* **119** (12), 8530–8551.

SAUERMANN, G., KROY, K. & HERRMANN, H. 2001 Continuum saltation model for sand dunes. *Phys. Rev.* E **64** (3), 031305.

SCHERER, M., KIDANEMARIAM, A.G. & UHLMANN, M. 2020 On the scaling of the instability of a flat sediment bed with respect to ripple-like patterns. *J. Fluid Mech.* **900**, A1.

SCHERER, M., UHLMANN, M., KIDANEMARIAM, A.G. & KRAYER, M. 2021 On the role of turbulent large-scale streaks in generating sediment ridges. *J. Fluid Mech.* **930**, A11.

SCHMEECKLE, M.W. 2014 Numerical simulation of turbulence and sediment transport of medium sand. *J. Geophys. Res.: Earth* **119** (6), 1240–1262.

SELMANI, H., VALANCE, A., OULD EL MOCTAR, A., DUPONT, P. & ZEGADI, R. 2018 Aeolian sand transport in out-of-equilibrium regimes. *Geophys. Res. Lett.* **45** (4), 1838–1844.

SEMINARA, G. 2010 Fluvial sedimentary patterns. *Annu. Rev. Fluid Mech.* **42** (1), 43–66.

SHIELDS, A. 1936 Anwendung der Aehnlichkeitsmechanik und der Turbulenzforschung auf die Geschiebebewegung. Mitteilungen der versuchanstalt für wasserbau und schiffbau, Technischen Hochschule Berlin.

STOESSER, T., BRAUN, C., GARCÍA-VILLALBA, M. & RODI, W. 2008 Turbulence structures in flow over two-dimensional dunes. *ASCE J. Hydraul. Engng* **134** (1), 42–55.

UHLMANN, M. 2005 An immersed boundary method with direct forcing for the simulation of particulate flows. *J. Comput. Phys.* **209** (2), 448–476.

UHLMANN, M. 2008 Interface-resolved direct numerical simulation of vertical particulate channel flow in the turbulent regime. *Phys. Fluids* **20** (5), 053305.

VALANCE, A. 2005 Formation of ripples over a sand bed submitted to a turbulent shear flow. *Eur. Phys. J.* B **45** (3), 433–442.

VOWINCKEL, B., KEMPE, T. & FRÖHLICH, J. 2014 Fluid-particle interaction in turbulent open channel flow with fully-resolved mobile beds. *Adv. Water Resour.* **72**, 32–44.

WONG, M. & PARKER, G. 2006 Reanalysis and correction of bed-load relation of Meyer-Peter and Müller using their own database. *ASCE J. Hydraul. Engng* **132**, 1159–1168.

YALIN, M.S. 1977 *Mechanics of Sediment Transport*, 2nd edn. Pergamon.

ZGHEIB, N. & BALACHANDAR, S. 2019 Linear stability analysis of subaqueous bedforms using direct numerical simulations. *Theor. Comput. Fluid Dyn.* **33** (2), 161–180.

ZGHEIB, N., FEDELE, J.J., HOYAL, D.C.J.D., PERILLO, M.M. & BALACHANDAR, S. 2018 Direct numerical simulation of transverse ripples: 2. Self-similarity, bedform coarsening, and effect of neighboring structures. *J. Geophys. Res.: Earth* **123** (3), 478–500.

ZILKER, D.P. & HANRATTY, T.J. 1979 Influence of the amplitude of a solid wavy wall on a turbulent flow. Part 2. Separated flows. *J. Fluid Mech.* **90** (2), 257–271.